Anna Seiwald, BSc.

Feasibility of quantitative susceptibility mapping in post-mortem myocardium

Master's Thesis

to achieve the university degree of

Diplom-Ingenieurin

Master's degree programme: Biomedical Engineering

submitted to

Graz University of Technology

Supervisor

Univ.-Prof. Dipl.-Ing. Dr.techn. Rudolf Stollberger

Institute of Medical Engineering
Head: Univ.-Prof. Dipl.-Ing. Dr.techn. Rudolf Stollberger

Advisor

Dr. Bridgette Webb, M.Sc.

Graz, December 2018

Statutory Declaration

I declare that I have authored this thesis independently, that I have not used other than the declared sources/resources, and that I have explicitly indicated all material which has been quoted either literally or by content from the sources used. The text document uploaded to TUGRAZonline is identical to the present master's thesis.

Date	Signature

Eidesstattliche Erklärung

Ich erkläre an Eides statt, dass ich die vorliegende Arbeit selbstständig verfasst, andere als die angegebenen Quellen/Hilfsmittel nicht benutzt, und die den benutzten Quellen wörtlich und inhaltlich entnommenen Stellen als solche kenntlich gemacht habe. Das in TUGRAZonline hochgeladene Textdokument ist mit der vorliegenden Masterarbeit identisch.

Datum	Unterschrift

Abstract

Quantitative Susceptibility Mapping (QSM) is a novel contrast technique enabled by post-processing MRI magnitude and phase images, which reveals the tissues underlying magnetic susceptibility property. In the presented work recently developed QSM algorithms were evaluated based on phantom MRI acquisitions with different sequences to provide information in terms of accuracy, precision and stability depending on the input sequence. The whole QSM workflow included MRI acquisitions with three different sequences, masking, executing the algorithm and image registration. Further, ex situ porcine hearts acquisitions serve for a better sequence evaluation with hearts embedded in air and water. The last ex situ porcine hearts experiments with hearts embedded in air, water, galden and agarose are dedicated to gain information about the influence of the embedding media on the calculated tissue's magnetic susceptibility in the myocardium. Overall, the work should give an overview of latest open-access QSM algorithms applied to myocardium acquisitions, trying to answer the question whether QSM is ready for a post-mortem application to serve as a tissue specific investigation method for myocardium alterations, for example the detection of myocardial infarctions.

Zusammenfassung

Quantitative Susceptibility Mapping (QSM) ist eine neuartige Kontrasttechnik durch die Nachverarbeitung von MRT Magnituden- und Phasenbildern, wodurch ein Bild basierend auf der zugrundeliegenden magnetischen Suszeptibilität des Gewebes entsteht. In der nachfolgenden Arbeit wurden aktuelle QSM Algorithmen anhand von Phantommessungen untersucht um diese in den Faktoren Genauigkeit, Präzision und Stabilität abhängig von der gemessenen Sequenz zu beurteilen. Der gesamte QSM Ablauf beinhaltet die MRT Datenaufnahme mit drei unterschiedlichen Sequenzen, Maskierung, Ausführen des Algorithmus sowie Bildregistrierung. Zusätzlich wurden Messungen mit ex situ Schweineherzen, eingebettet in Luft und Wasser durchgeführt um den Einfluss der Sequenz besser zu beurteilen. Zuletzt wurden Schweineherzen in den Substanzen Luft, Wasser, Galden und Agarose eingebettet um den Einfluss der Umgebungssubstanz auf die magnetische Suszeptibilität des Myokardiums zu untersuchen. Zusammenfassend gibt die Arbeit einen Überblick über aktuelle QSM Algorithmen angewendet auf Messungen des Myokards, wobei die Frage beantwortet werden soll, ob QSM aktuell eine post-mortem Anwendung finden kann und dabei als gewebespezifischer Marker zur Erkennung von Myokardveränderungen fungieren kann.

Acknowledgment

I want to thank my supervisors, Univ.-Prof. Dipl.-Ing. Dr.techn. Rudolf Stollberger and Dr. Bridgette Webb, M.Sc. for their support.

Thanks to the Ludwig Boltzmann Institute, Mag. Dr. Reingard Riener-Hofer, for making this work possible and supporting me via the FemTech internship. Also, I want to thank my office colleagues Sylvia, Hanna and Bernhard for their assistance during the internship.

Thank you Bridgette for everything, for your time, encouragements and inputs, it was a pleasure to work with you.

Teresa, thanks for your help, funny and inspiring talks in the last ten years. I could not have imagined a better school and study buddy.

Last but not least I want to thank my parents for their unconditional support throughout my education, especially in the last year, supporting me in whatever I pursue.

Contents

List of Figures

List of abbreviations

QSM	Quantitative Susceptibility Mapping
GRE	Gradient recalled echo
TE	Echo time
TR	Repetition time
RF	Radiofrequency
FID	Free induction decay
EPI	Echo planar imaging
ROI	Region of interest
FOV	Field of view
SNR	Signal-to-noise ratio
RSD	Relative standard deviation
PMMR	Post-mortem MRI

1 Introduction

Quantitative Susceptibility Mapping (QSM) is a novel contrast technique based on MRI acquired magnitude and phase images. It reveals the underlying tissues magnetic susceptibility property, which describes the materials interaction with an applied magnetic field. The detection of hemorrhagic myocardial infarction and small tissue alterations in the myocardium is a complex and challenging topic. QSM has the potential to serve as an investigation method for intramyocardial hemorrhages, as the different states of hemoglobin differentiate in their susceptibility. When unpaired electrons are present, the susceptibility property is paramagnetic, whereas diamagnetic hemoglobin has no unpaired electrons [1, 2].

The presented work investigates the influence of MRI scan parameters, reconstruction algorithms and embedding medias on quantitative susceptibility maps in ex vivo tissue. Since there is almost no literature on QSM for the myocardium, the expected susceptibility values are unknown. Recent work by Dibb et al. [3] investigated susceptibility values of a mouse heart specimen and resulted in values around $-30ppm$ to $30ppm$. The basis of the given work are phantom acquisitions, with vials embedded in agarose containing a Magnevist® solution (Bayer Vital, company). It was used for the algorithm and accuracy evaluation as well as repeatability and reproducibility analysis. Further evaluations were done with acquisitions of ex vivo porcine hearts.

In MRI acquisitions, the magnitude and phase images can be obtained by a MR gradient recalled echo (GRE). Magnitude images are based on underlying tissue property, where the contrast is dependent on proton density, T1, T2 or T2* relaxation. On the other hand in phase images, contrast is based on the local precession frequencies.

The local chemical shift $\sigma(\vec{r})$ and the magnetic field perturbations contributes to local Larmor resonance frequency shifts $\Delta f(\vec{r})$ (Equation 1.1) [4].

$$\Delta f(\vec{r}) = -\gamma \left[B^{\Delta}(\vec{r}) - \sigma(\vec{r}) \right] / (2\pi) \tag{1.1}$$

In tissues, the local magnetic field perturbation is given as the convolution of the susceptibility distribution with a dipole field. When only considering magnetization along z-direction due to an orientation along the main magnetic field the local magnetic field is given by Equation 1.2, where components orthogonal to the z-direction are neglected. $\Theta_{rr'}$ is the angle between $r - r'$ and z, $\vec{B}0$ is a static magnetic field. [5, 6, 4].

$$B^{\Delta}_{z,local}(\vec{r}) = |\vec{B}_0| \int_{r' \neq r} \chi(\vec{r}') \frac{3 \cdot cos^2(\Theta_{rr'}) - 1}{4\pi |\vec{r}' - \vec{r}|^3} d^3 r' \tag{1.2}$$

The frequency shift can be defined by the echo time dependent phase of a GRE, where $\phi^0(\vec{r})$ equals the phase at TE = oms (Equation 1.3) [4].

$$\Delta f(\vec{r}) = \frac{\phi^{TE}(\vec{r}) - \phi^0(\vec{r})}{2\pi TE} + \Delta f_{ref,0} \tag{1.3}$$

$\Delta f_{ref,0}$ is the difference between the Larmor frequency of the main magnetic field and the reference frequency of the MR system (demodulation frequency) [4, 7]. In literature the term is often omitted. Rearranging Equation 1.3 results in an echo time-dependent phase term (Equation 1.4) [4, 7].

$$\phi(TE) = \phi^0 + 2\pi \cdot \Delta f(\vec{r}) \cdot TE \tag{1.4}$$

Thus, the phase reflects the underlying susceptibility distribution $\chi(\vec{r})$.

If the phase changes exceed the interval of $(-\pi, +\pi)$, the phase is *wrapped* into this interval.

Equation 1.4 states that the phase contrast increases linearly with the echo time, against the exponential increase of noise with increasing echo time in

the high-SNR regime. As a result, the maximum contrast in phase images is when $TE = T2^*$ [7, 8].

Since magnitude and phase images are based on different underlying tissue parameters, both contain information about different anatomic structures or physiological properties [8].

The magnetic susceptibility is a material's property which describes the materials interaction with an applied magnetic field. These interactions are field perturbations, which can be measured with the phase of a GRE sequence. The magnetic susceptibility χ is a dimensionless property. In Equation 1.5 H is the applied magnetic field and M the induced magnetization [9, 7].

$$M = \chi H \tag{1.5}$$

A material's susceptibility can be divided into four categories, diamagnetic, paramagnetic, superparamagnetic and ferromagnetic [10]. In diamagnetic materials the external field is weakened by an internal field which is aligned in the opposite direction to the external one. The susceptibility value χ is negative. In paramagnetic substances the opposite phenomenon takes place. The positive magnetic susceptibility leads to an amplification of the external magnetic field. When a material's property is between paramagnetic and ferromagnetic, it is described as superparamagnetic (e.g. iron oxide particles). Finally, ferromagnetic materials have a high positive magnetic susceptibility which leads to a high bulk magnetic moment when placed in a magnetic field [11, 12].

As previously mentioned, GRE sequences enable the reconstruction of both magnitude and phase images, where the phase is dependent on the gyromagnetic ratio (γ), the induced magnetic field (ΔB) and the time of the measurement (see Equation 1.6).

$$\phi = -\gamma \Delta B t \tag{1.6}$$

The susceptibility induced field perturbations can be calculated using the Fourier transform of the susceptibility distribution. k_z refers to the z-component of k-space and $K^2 = k_x^2 + k_y^2 + k_z^2$ (eq. 1.7). The inverse relation

between the susceptibility distribution and the measured phase is then given in Equation 1.8 [13].

$$\phi = -\gamma * B_0 * TE * FT^{-1} \left[\left(\frac{1}{3} - \frac{k_z^2}{K^2} \right) * FT(\chi_{Distribution}) \right] \tag{1.7}$$

$$\chi = FT^{-1} \left[FT \left(\frac{\phi}{-\gamma * B_0 * TE} \right) * \left(\frac{1}{\frac{1}{3} - \frac{k_z^2}{K^2}} \right) \right] \tag{1.8}$$

The k-space filter is equal to zero where $K^2 = 3k_z^2$, which is called the magic angle, 54.7°, making the problem ill-posed. By discretization, the ill-posedness can be overcome [14].

Another approach to overcome this problem is to sample at multiple orientations referred as COSMOS ("Calculation of susceptibility through multiple orientation sampling"), resulting in an unique solution. Therefore the object of interest needs to be reoriented in the MRI in relation to the main magnetic field. Although this method leads to an accurate solution, the reorientation of the object and necessity of multiple acquisitions as a whole is an impracticable method for clinical purposes [15].

To avoid problems by a denominator close to zero, truncating the dipole kernel leads to an alternative solution, where an acquisition at a single orientation is taken into account [16, 17].

The solution of the ill-posed inverse problem can also be achieved by using a regularization, for example Tikhonov regularization or a l_1-norm promoting sparsity [14].

In the following work the sequences used are introduced in Chapter 2. Chapter 3 is dedicated to the entire QSM workflow, which was used through all experiments. It includes sequence parameters as well as algorithm application information. Subsequent chapters are based on different acquisitions and their results. The basis is done by phantom and ex situ porcine hearts acquisitions in Chapter 4 comparing three recent QSM algorithms to investigate their accuracy, precision and stability depending on the input sequence. Based on the results, the acquisitions in Chapter 5 demonstrate

the potential influence of embedding media of an ex situ porcine heart during the MRI acquisitions on the resulting quantitative susceptibility map. The final Chapters 6 and 7 summarize the presented work and try to answer the question, whether QSM is ready for a post-mortem application.

2 MR Sequences used for data acquisition

2.1 Introduction

Pulse sequences control the timing of radiofrequency (RF) pulses, gradient applications and intervening time periods and are used to generate images with different contrast weightings. The GRE pulse sequence is controlled by two timings, the echo time (TE) and the repetition time (TR), usually given in ms. Further, the flip angle flips the protons from the longitudinal to the transversal plane by using a RF pulse. The type of the GRE and these parameters, which can be set by the user, achieve different image contrasts. TR defines the time between two RF pulses or the time between two consecutive repetitive time points and determines the effect of longitudinal relaxation on image contrast. TE specifies the time between the RF pulse excitation and the center of the echo read out. As the amount of transverse magnetization decays with time constant T2, TE controls the influence of T2 relaxation on image contrast [18, 19, 20, 21].

2.1.1 Gradient recalled echo (GRE)

The gradient recalled echo uses a three gradients in x, y and z-direction for spatial encoding. With an applied gradient the frequency in the MR signal changes, where the spins begin to dephase. The sequence diagram can be seen in Figure 2.1. The gradient from $t = 0$ to $t = \tau$ dephases the spins with an external dephasing gradient (Figure 2.1 c). The dephasing can be seen as a manipulation of the FID, which leads to a faster dephasing than the

natural dephasing with the T2 constant of the object. When reversing the gradient at time $t = \tau$ the dephasing process is reversed and the spins are starting to rephase (Figure 2.1 c). The gradient reverses the spins frequency, the ones which were precessing at a lower frequency are now precessing with a correspondingly higher frequency and vice versa. At time $t = 2\tau$ the gradient recalled echo is formed. At this point the gradients cumulative area is zero. For $t > 2\tau$ as the gradient persits, the spins are dephasing again (f). The rephasing gradient only affects spins that were initially dephased by the first gradient, so it does not refocus spins which dephased due to field inhomogeneities or spin-spin relaxation. This leads to a T2* contrast instead of T2. In comparison to the spin-echo, GRE sequences require only one RF pulse which means that the echo is formed faster. Therefore TE is shorter than in the spin-echo, which enables shorter repetition times [22, 23, 24, 25].

$$S_{GE} = S_0 \cdot e^{-\frac{TE}{T2^*}} \tag{2.1}$$

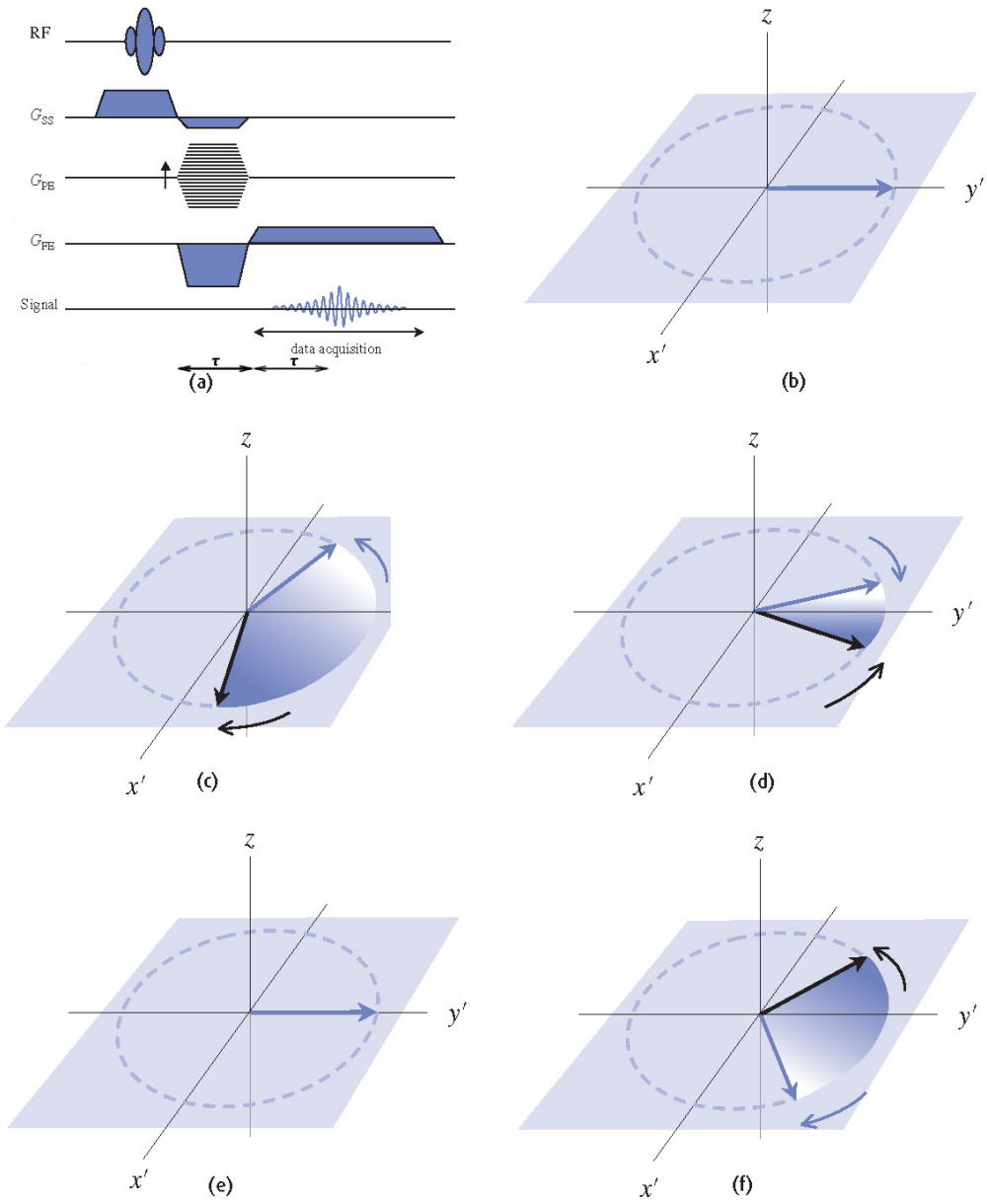

Figure 2.1: Basic gradient recalled echo. Modified from [22, 23].

2.1.2 Echo Planar Imaging (EPI)

Basically an echo planar imaging sequence is a technique where a 2D planar image can be acquired with a single or a small number of excitations. Due to this, a 2D image can be acquired in 50 to 100ms which reduces the effects of motion. In the single-shot GE-EPI the whole k-space is filled with one excitation pulse, a selective excitation pulse producing a FID signal, which is followed by a train of gradient echoes (Figure 2.2). Simultaneously to an oscillating frequency encoding gradient, the phase encoding gradient is increased by a constant amplitude for each acquired line in the k-space [26, 27]. This means that each line in the k-space is acquired at a different echo time. The signals amplitude $S(n)$ can be found in Equation 2.2. The parameter n refers to the echo index in the echo train, S_0 is the signals amplitude at $t = 0$ [28]. The term EPI factor (e.g. Siemens MRI scanners) corresponds to the number of k-space lines acquired with one excitation [27].

$$S_{GE\_EPI}(n) = S_0 \cdot e^{-\frac{TE(n)}{T2^*}} \tag{2.2}$$

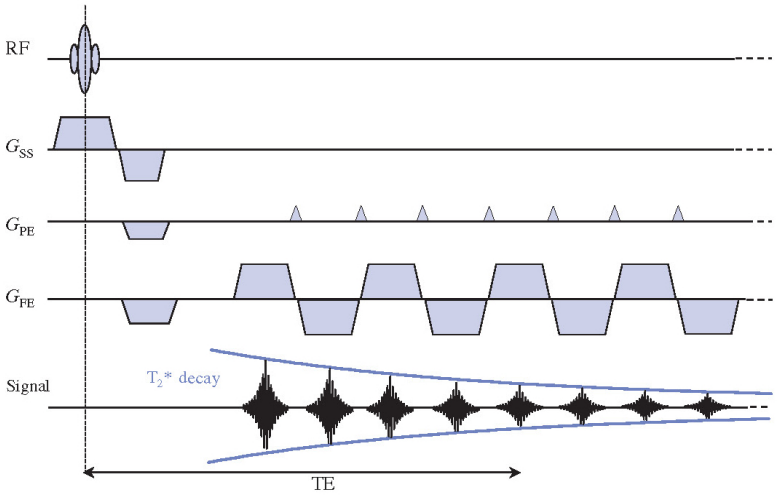

Figure 2.2: Basic GE-EPI [26].

3 Established methods for data acquisition and analysis of phantom and ex situ porcine hearts experiments

3.1 Introduction

This chapter describes the MR sequences and parameters which enable the acquisition of the magnitude and phase images required for QSM. Additionally the most recent developments in terms of algorithms for the reconstruction of quantitative susceptibility maps are given.

Three data acquisition strategies were applied, meaning that differences in acquisition time are present. A short description of the pulse sequences can be found in Chapter 2.

The latest QSM algorithms (*MEDI, starQSM*) use a calculation procedure which includes phase unwrapping, background field removal and in a final step solving the phase to susceptibility inverse problem (Figure 3.1). In the presented work three QSM algorithms which are based on single-orientation MRI acquisitions were used. The *MEDI* algorithm [6, 29], which incorporates morphological information, the *starQSM* algorithm [30], which uses a two level regularization approach and the *TGV* algorithm which is based on a total generalized variation method [31, 32].

For data reconstruction a mask of the investigated object is used as input. As seen in Figure 3.1, the TGV algorithm uses phase images and the mask

as input, where the MEDI and starQSM algorithms additionally require magnitude images.

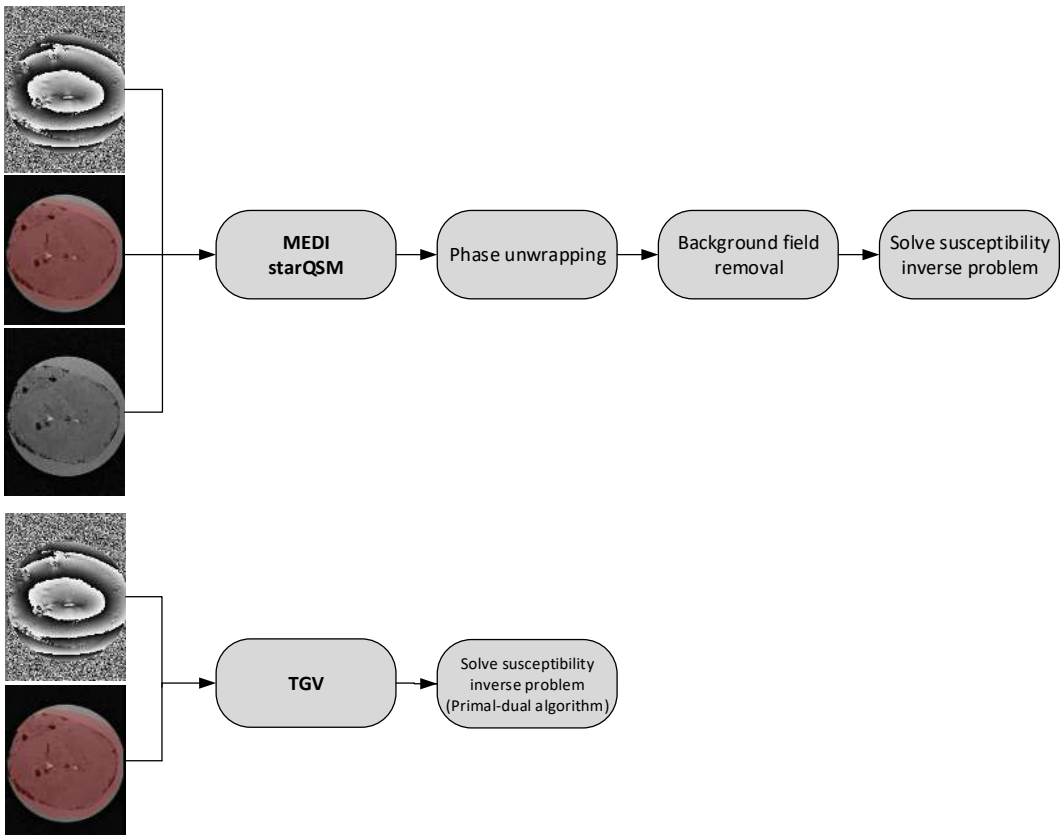

Figure 3.1: Workflow of QSM algorithms, MEDI and starQSM algorithm are split into three steps using magnitude images, phase images and a mask data. The TGV algorithm solves the inverse problem with a single optimization step using phase images and a mask.

Overall, the whole QSM-workflow in the presented work consisted of the following steps. At first, MRI image acquisition leading to magnitude and phase images. Second step, masking of the desired object with ITK-Snap followed by the calculation of the quantitative susceptibility map with one of the algorithms. If necessary, image registration because of slightly different image acquisition parameters of the single and multi-echo GRE and EPI sequence or reorientation of the measured object was done using

SimpleElastix [33]. After that, the analysis of selected regions of interests (ROIs) was done with ITK-Snap [34], MATLAB and R. ITK-Snap was used for selecting the ROIs on the 3D dataset, MATLAB for extracting the voxel values out of the dataset given by the mask drawn with ITK-Snap. Finally, the software R was used for statistical calculations and evaluations.

3.2 Data acquisition

For data acquisition, single and multi-echo GRE sequences as well as a EPI sequence were used. The sequences were chosen to have a basis for a sequence evaluation. As the sequences differ substantially in their data acquisition, they also differ in their image acquisition time. Details of the sequences can be found in Chapter 2 with their parameters given in Tables 3.1, 3.2 and 3.3. The TE of the single echo GRE was selected to match the T2* of post-mortem ex situ porcine hearts [35]. The spatial resolution was based on past cardiac post-mortem studies [36, 37]. To generate the quantitative susceptibility map for the multi-echo data with the TGV algorithm, the maps were generated for each echo for echoes 2 to 9 and then the mean map was calculated. All acquisitions were carried out at room temperature. In all experiments a 20 channel head coil was used for data acquisition.

Sequence	TE (ms)	TR (ms)	Flip angle (°)	FOV (mm)	Voxelsize (mm^3)	Acquisition time (mm:ss)	Number of slices
3D Multi-echo GRE	3.09/8.55/ 13.84/19.13/ 24.42/29.71/ 35.00/40.29/ 46.56/57.71/ 68.86/80	85	27	164x250	0.65x0.65x1.5	18:41	88

Table 3.1: Sequence parameters multi-echo GRE.

Sequence	TE (ms)	TR (ms)	Flip angle (°)	FOV (mm)	Voxelsize (mm^3)	Acquisition time (mm:ss)	Number of slices
3D Single echo GRE	40	60	23	164x250	0.65x0.65x1.5	13:11	88

Table 3.2: Sequence parameters single echo GRE.

Sequence	TE (ms)	TR (ms)	Flip angle (°)	FOV (mm)	Voxelsize (mm^3)	Averages	Epifactor	Acquisition time (mm:ss)	Number of slices
3D EPI	21	57	10	175x280	0.729x0.729x1.5	3	9	08:02	88

Table 3.3: Sequence parameters EPI.

3.3 Segmentation

To generate a mask of the hearts myocardium in the 3D datasets the free software ITK-SNAP [34] was used. For the hearts embedded in water the masking included some of the water surrounding it. Hearts surrounded by air were segmented using a semi-automatic masking approach. A coarse segmentation was done with the Active Contour Segmentation Mode (SNAKE) in ITK-SNAP which uses a thresholding method for a coarse presegmentation. The fine segmentation was manually performed by hand using the paintbrush mode. In the experiments with hearts in different embeddings in Chapter 5 the segmentation only included the myocardium and was also done partly automated and partly manually.

3.4 Image Registration

SimpleElastix [33] efficiently achieved the desired result after a few lines of code. When defining the fixed and moved images for the registration, the transformation parameter map was automatically generated and applied to register images into the same image space. This enabled a more robust ROI-based evaluation of MR sequences and QSM algorithms. Due to slightly different voxel sizes and field of views (FOV) of the EPI data and the single and multi-echo data, the GRE data were registered to the EPI data, which means that the higher resolution acquisitions were registered to the lower acquisitions. The image registration process was performed with magnitude images and then applied to the corresponding reconstructed susceptibility maps.

3.5 Image analysis

The software ITK-Snap [34] was also used for image evaluation with specific ROIs. Further analysis of voxel values was done with MATLAB and the statistics software R. In all ROIs in ex vivo data, outliers were removed by using the 1.5IQR rule. The interquartile range is defined as $Q_3 - Q_1$, which can be used for applying the 1.5IQR rule, stating that in each ROI, data points 1.5xIQR below the lower quartile and 1.5xIQR above the upper quartile were considered as outliers and removed [38].

Application of the 1.5IQR rule is valid under the assumption that the underlying data follows a normal distribution. To test for normality, the Shapiro-Wilk test was applied to ROIs which contained 90 data points. As seen in Figure 3.2, all p-values are greater than 0.05, meaning there is no significant evidence against the hypothesis that the underlying data follows a normal distribution. When applying the 1.5IQR rule, approximately 1.7% to 2.5% of the pixel values were marked as outliers and removed.

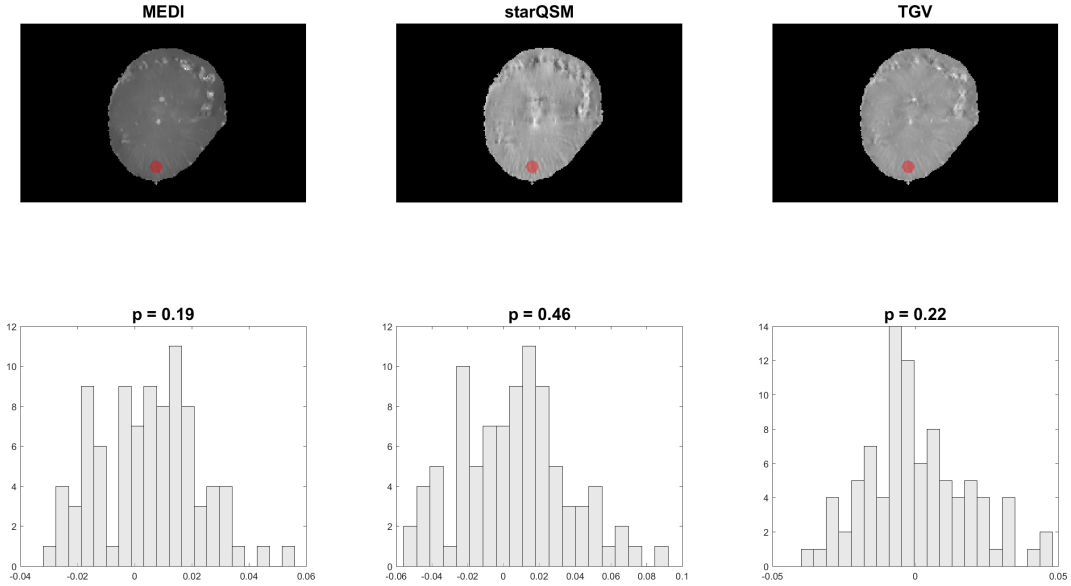

Figure 3.2: Test for normality with Shapiro-Wilk test. p-values with corresponding histograms.

3.6 QSM algorithms

As already mentioned, the three algorithms used are based on different approaches.

3.6.1 MEDI

To overcome the ill-posedness of the susceptibility problem, the MEDI algorithm utilizes the fact that the magnitude image and the susceptibility map should consist of similar structures. The approach is that regions with uniform intensity in the magnitude image also represent regions with an uniform underlying susceptibility. Therefore the edge information of the magnitude image should delineate these regions. The solution should minimize streaking artifacts which originate at tissue boundaries. Voxels of the susceptibility map that are not on the magnitudes image gradient are minimized, accomplished with a L_1-norm [6, 29]. The algorithm is based on a open source MATLAB code which uses dicom magnitude and phase images as input. The calculation incorporates multiple steps, phase unwrapping with a region growing algorithm, background field removal by projection onto dipole fields [39, 29] and finally the MEDI_L1 algorithm [40, 41, 6, 42, 29]. If the MEDI algorithm is used for brain data, optionally a mask of the cerebrospinal fluid (CSF) region can be provided. When using it, the variance within the reference region is penalized and at the end of the calculation the mean susceptibility within this region is subtracted of all pixel values. The calculated susceptibility values within the image can then be reported as "referenced with respect to ventricular CSF" for example. Unfortunately this feature is currently only available for brain data. The functions and algorithm can be downloaded via the Cornell MRI Research Lab `http://pre.weill.cornell.edu/mri/pages/qsm.html`. The algorithm was tested on MATLAB 2009a.

3.6.2 starQSM

When there are local high susceptibility values present, algorithms tend to display severe streaking artifacts in the reconstruction. One attempt to reduce these artifacts is a two level approach such as that used by the starQSM algorithm. There the reconstruction uses one regularization parameter for large and small susceptibility values. It uses a L2 as a data consistency term and a L1 as a regularization term (TV). First, strong susceptibility values are calculated with a large TV weighting parameter. The dipole field of the strong susceptibility sources is then calculated with the forward equation and subtracted from the total phase. The second step is the calculation of smaller susceptibility sources with the remaining phase using a smaller TV weighting parameter. The final result is a superposition of these two values [30]. The starQSM algorithm is embedded in the STI Suite which can be obtained via `https://people.eecs.berkeley.edu/~chunlei.liu/software.html`. The algorithm calculation is guided through a graphical user interface starting in MATLAB. At first, images are loaded, where three different datatypes are accepted. Both magnitude and phase images are required in .mat, DICOM or NIFTI format. When loading dicom files the input parameters (voxel size, echo times and magnetic field direction) are loaded automatically. Masking can be done with the integrated intensity based thresholding tool or by loading a segmentation as a .mat- or NIFTI-file. The last two steps include the phase processing [43, 44] and finally the starQSM algorithm [30, 45]. In contrast to the MEDI algorithms MATLAB files, the STI Suite files are p-files, which means that the code is obfuscated and cannot be changed or displayed.

3.6.3 TGV

The TGV based reconstruction technique combines the steps for phase unwrapping, background field removal and dipole inversion into a single integrated step. While TV assumes that the underlying image is piecewise constant, leading to staircase artifacts if this is not the case, the TGV based approach prefers piecewise smooth images and is therefore better suited for the given problem. Due to the fact that the algorithm incorporates multiple

steps into a single optimization step, error propagation is reduced what makes the algorithm more robust [31, 32]. The TGV is written in python and can be downloaded at the Neuroimaging Research Unit of Graz at http://www.neuroimaging.at/pages/qsm.php. When using it under linux the installation is easy with a provided setup file. The algorithm is executed with a single command line starting with *tgv_qsm* giving the phase image (indicated by *-p*), a mask image (*-m*), both as NIFTI-files. Further the used echo time is given in seconds and the fieldstrength in Tesla. Example algorithm call: *tgv_qsm -p Heart_single-echo_phase.nii.gz -m Segmentation_Heart_single-echo.nii.gz -f 3.0 -t 0.021 -s -e 0 –ignore-orientation*.

4 Evaluation of data acquisition and analysis strategies for QSM ex situ porcine hearts

4.1 Introduction

Initially state-of-the-art open access QSM algorithms MEDI, starQSM and TGV were evaluated.

Phantom acquisitions and additionally acquisitions on five ex situ porcine hearts were performed. The objects were scanned with three different sequences each (Tables 3.1, 3.2 and 3.3). The results provided information regarding the QSM algorithms in terms of accuracy, precision and stability depending on the input sequence. With the ex situ porcine heart acquisitions sequences were evaluated with a single algorithm to achieve a preliminary comparison of two different embedding medias, air and water.

4.2 Methods

4.2.1 Phantom experiment

The phantom was designed to be motion insensitive (Figure 4.1a) with vials containing different solution concentrations, embedded in a 1.7% agarose gel in a glass jar. The solutions in the vials were different concentrations of the Magnevist® solution (Bayer Vital, company). The concentrations and their corresponding susceptibility values can be found in Table 4.1. The

phantom susceptibility values are based on previous published work with phantom measurements for the starQSM and MEDI [46, 30]. When assuming susceptibility values of $-30ppm$ to $30ppm$ as given work by Dibb et al. [3], then the phantoms susceptibility values are beyond this interval, but they cover the clinical value range.

The vials were approximately 12cm long with a diameter of 15mm and a wall thickness of 1mm. For the calculation of the phantom a molar concentration of $c = 0.5mmol/ml$ for the undiluted Magnevist was used [47] and a susceptibility of $326ppml/mol(293K)$ was assumed [48]. Equation 4.1 shows the calculation of the susceptibility for a 100% Magnevist® concentration. The highest concentration of the phantom was 1%. Since the solutions concentrations were halved, also the corresponding susceptibility values are halved, resulting in a linear relationship (Table 4.1). The vials volume was 15ml, whereby the highest concentration of 1% contained $150\mu l$ of Magnevist®. Table 4.1 shows the calculated concentrations, desired volumes for pipetting and real pipetted volumes with real concentration volumes values given in the right column. For the dilution of Magnevist distilled water was used. Due to an error during pipetting, the vial one (Figure 4.2) was excluded from the evaluation (grayed out).

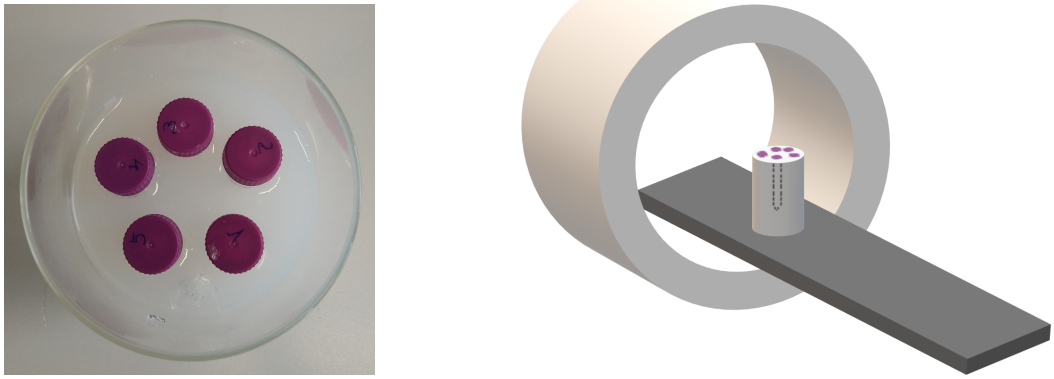

(a) Phantom setup vials embedded in agarose bird's eye view.

(b) Phantom's orientation in the MRI.

Figure 4.1: Phantom setup and orientation.

An example of the masking for the susceptibility evaluation can be found in Figure 4.2. The ROIs consisted of one slice of voxels with 121 voxels for EPI and 148 voxels for single and multi-echo echo data in each vial. For a better comparison of the algorithms, all susceptibility values were referenced to the mean of voxels in the center of the phantom, which consisted of agarose gel. Therefore all calculated voxel susceptibility values were subtracted by the mean of a center region, drawn in purple in Figure 4.2a. The reference region was drawn across 13 slices with the shape shown in 4.2b.

$$\begin{aligned} \chi &= 326ppm\frac{l}{mol} \cdot c = \\ &= 326ppm\frac{l}{mol} \cdot 0.5\frac{mol}{l} = 163ppm \end{aligned} \tag{4.1}$$

desired concentration (%)	**desired Magnevist® volume (μl)**	**real Magnevist® volume (μl)**	**real concentration (%)**	χ **ppm**
1	150	150	1	1.63
0.5	75	75	0.5	0.815
0.25	37.5	37	0.246	0.401
0.13	18.75	19	0.126	0.205
0.062	9.375	9.3	0.062	0.101

Table 4.1: Phantom susceptibilty values.

In the MRI scanner, the phantom was aligned perpendicular to $B0$. A graphic representation of the orientation can be found in Figure 4.1b. It was measured three times (named as 1a, 2a and 2b), whereby it was taken out of the isocenter between the first two measurements. Therefore statements about the algorithms reproducibility (1a $\leftrightarrow$ 2a) and repeatability (2a $\leftrightarrow$ 2b) can be made.

As a basis for comparison of the sequences, the signal-to-noise ratio (SNR) of the magnitude images in each vial was calculated. The calculation uses two phantom acquisitions (2a, 2b) and is based on equations in [49]. The signals histogram and the histogram of the difference image (noise) should

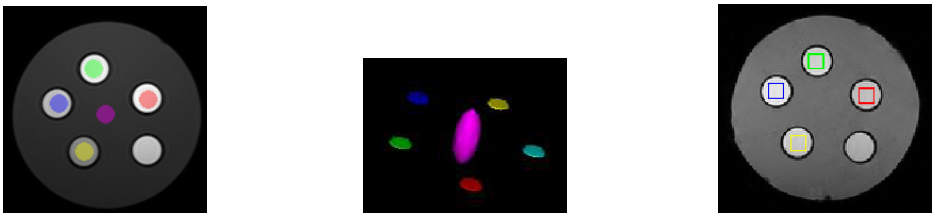

(a) Masking of ROIs in the vials.

(b) Masking of ROIs in the vials.

(c) Masking of ROIs signal and noise for SNR calculations.

Figure 4.2: Phantom masking and SNR ROIs.

follow a Gaussian distribution [49], given in Figure 4.6. Example ROIs can be found in Figure 4.2c. For the multi-echo data the echo number 8 was taken, which corresponded to an echotime of $TE = 40.29ms$ (Table 3.1).

To compare the sequences in terms of significant differences in the selected ROIs, a Welch t-test (no assumption of equal variance) was used. The significance level was set to $\alpha = 0.05$. The relative standard deviation (Equation 4.2) was also calculated for each sequence and phantom susceptibility value.

$$RSD\% = \frac{100 \cdot std(x)}{\bar{x}} \tag{4.2}$$

Bland-Altman plots serve as a further evaluation for repeatability and reproducibility. In the plots the 95% limits of agreement [50] are marked which are calculated by Equation 4.3.

$$LoA = \bar{x} \pm 1.96\sigma \tag{4.3}$$

For an accuracy evaluation the relative error E_r was calculated by Equation 4.4, which results in an error given in %. The variable x indicates the expected value, x_m the calculated value.

$$E_r = \frac{x - x_m}{x} \cdot 100 \tag{4.4}$$

4.2.2 Porcine ex situ hearts experiments

In addition to phantom acquisitions the algorithms were also tested on data from ex situ porcine hearts. Freshly excised hearts were used and data acquisition took place within 15 hours after heart excision. As the best contrast in phase images is achieved with $TE = T2^*$ (Chapter 1) the sequence parameters were selected to follow this requirement. Relating to earlier studies the $T2^*$ of ex situ porcine hearts was found to be around $40ms$ [35]. To create a consistent measurement setup, the ex situ porcine hearts acquisitions were performed in a glass jar (Figure 4.5), with the same size as for the phantom. The cylindric glass jar had a diameter of 10.4cm and a height of 20.2cm, enabling it to fit in the MRI head coil. During data acquisition the hearts were surrounded by tap water. To keep the heart from floating upwards a soft synthetic block was used to hold it down. The masking of the hearts which was used for the algorithms included some of the water in the jar (Figure 4.3). In contrast to the phantom measurement setup, the real underlying tissue susceptibility of the hearts is unknown, leading to alternative analysis of the results. Error bar plots provide an overview of the agreement of the different algorithms when using varying input sequences.

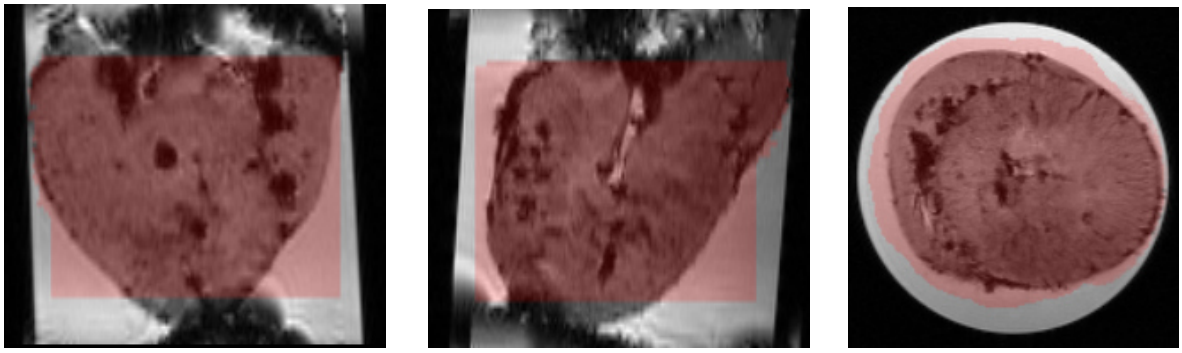

Figure 4.3: Heart 1 masking, single echo data, approximate 4 Chamber/2 Chamber view.

For the sequence evaluation the measurement setup was similar to that of the algorithm evaluation. Again using the glass jar, three hearts were embedded in air and water each. For a comparison of the sequences, violinplots show the susceptibility values for different ROIs. For each heart three ROIs

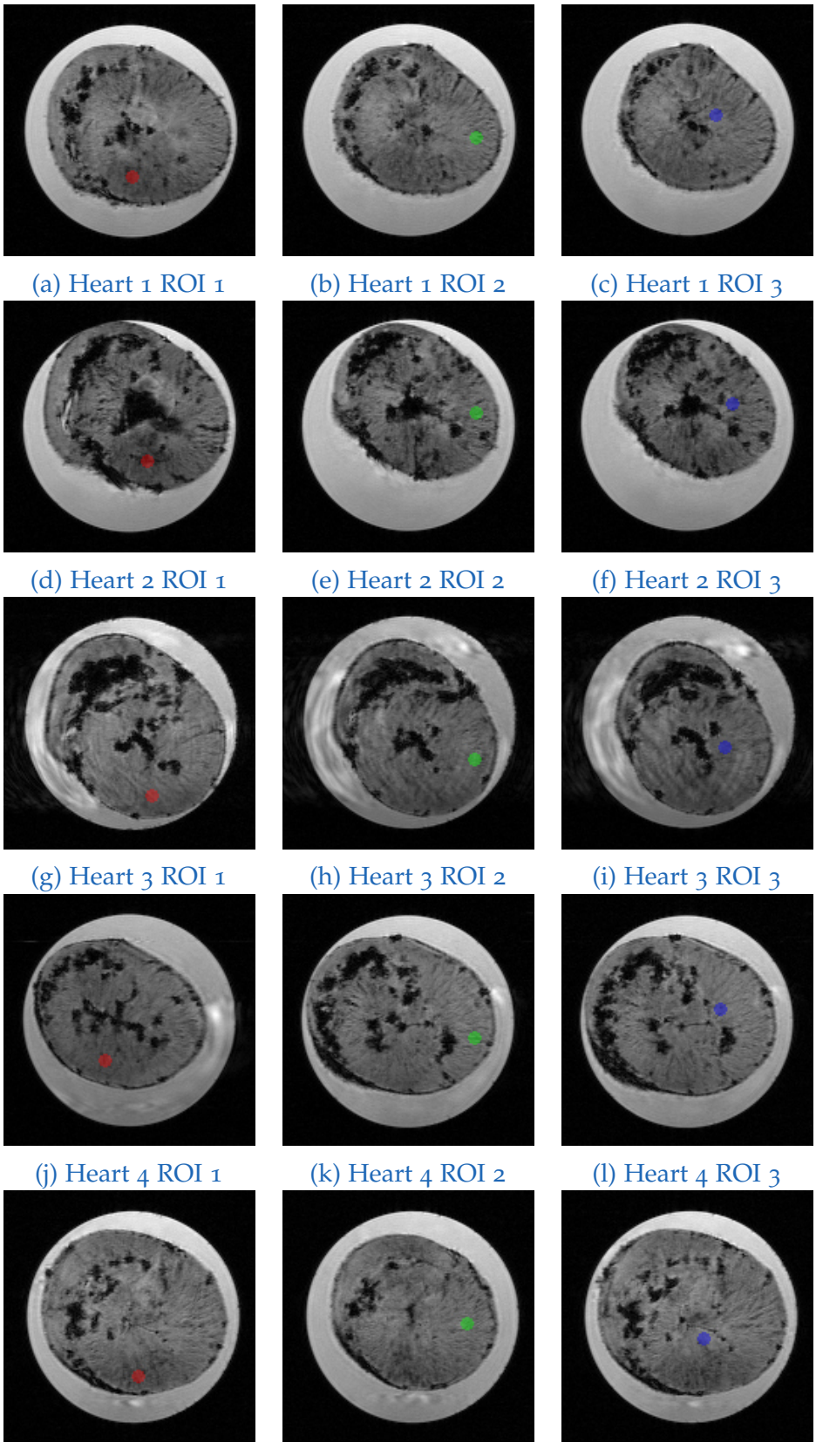

(a) Heart 1 ROI 1 (b) Heart 1 ROI 2 (c) Heart 1 ROI 3

(d) Heart 2 ROI 1 (e) Heart 2 ROI 2 (f) Heart 2 ROI 3

(g) Heart 3 ROI 1 (h) Heart 3 ROI 2 (i) Heart 3 ROI 3

(j) Heart 4 ROI 1 (k) Heart 4 ROI 2 (l) Heart 4 ROI 3

(m) Heart 5 ROI 1 (n) Heart 5 ROI 2 (o) Heart 5 ROI 3

Figure 4.4: Single echo GRE magnitude images and corresponding ROIS.

were evaluated which are located in segments the myocardium, see Figure 4.4. ROI placement was in the normal appearing myocardium by avoiding large vessels or other local air or fluid sources to avoid local susceptibility influences by them. Due to the fact that outliers were removed in all evaluated ROIs, the sample size differs for each ROI and sequence. Welch t-test was used to determine, whether there was a significant difference between the susceptibility values when the hearts were embedded in air or water. For the Welch t-test the significance level was set to $\alpha = 0.05$. For further statistical evaluation the post-hoc Tukey test for ANOVA was used, which compares the sequences pairwise in terms of significant differences. Compared to the evaluation with the Welch t-test, the Tukey's test did not compare each ROI separately, instead all ROIs from all three hearts for air and water were summarized.

Figure 4.5: Ex situ porcine heart acquisition setup (air).

4.3 Results

4.3.1 Image Quality in phantom experiments

The signal and noise distributions for the phantom ROIs marked in Figure 4.2c are shown in Figure 4.6, with the corresponding SNR values given in Table 4.2. The SNR values of the EPI and single echo sequence are in all four ROIs higher than the values for the multi-echo sequence.

	SNR			
	ROI1	**ROI2**	**ROI3**	**ROI4**
EPI	160.81	178.90	187.40	152.20
multi-echo	138.18	142.79	117.78	131.46
single echo	143.05	171.19	204.96	171.30

Table 4.2: SNR values for each sequence and ROI.

Figure 4.7 shows the resulting quantitative susceptibility maps of the phantom for the three sequences and algorithms. All images are scaled to display susceptibility values from $-0.5ppm$ to $0.5ppm$. As mentioned in 4.2 data normalization was performed (Figure 4.8). All algorithms show artifacts, whereby the MEDI algorithm suffers the most from streaking artifacts.

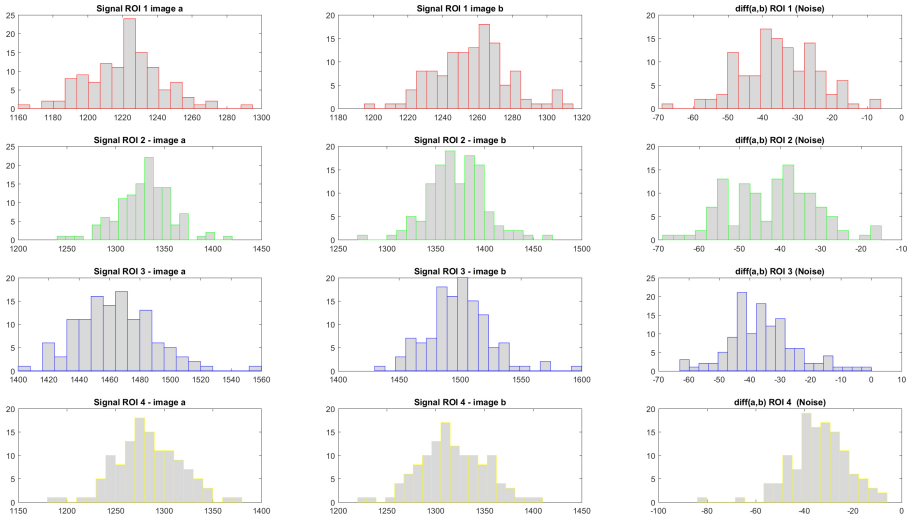

(a) EPI

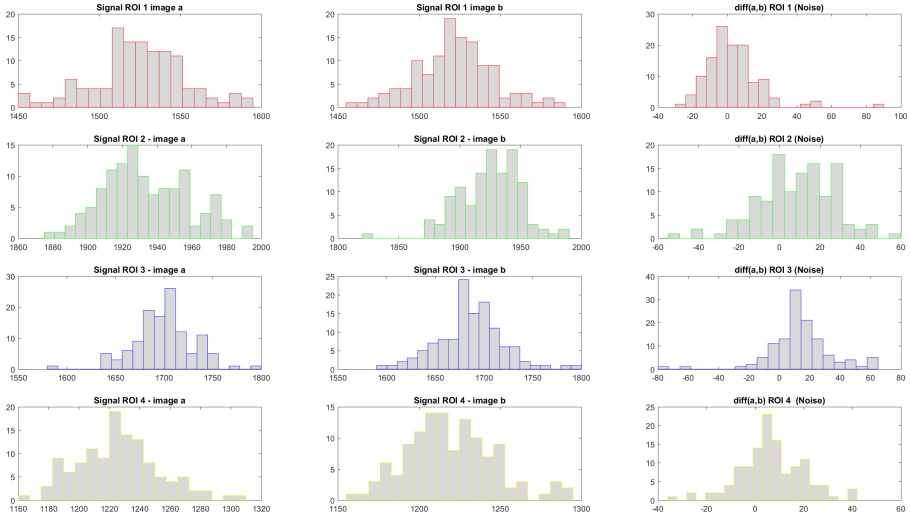

(b) multi-echo, echo 8, $TE = 40,29ms$

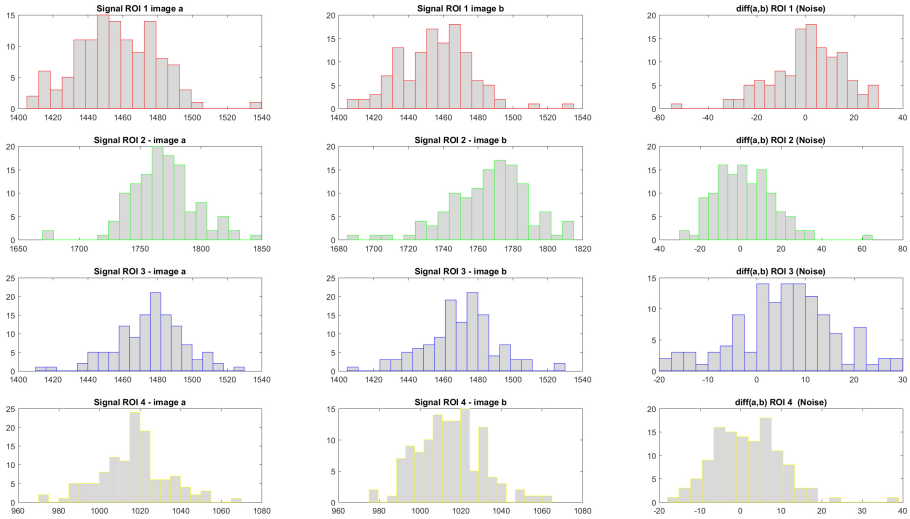

(c) single echo

Figure 4.6: Phantom histograms for each sequence, ROIs according to Figure 4.2c.

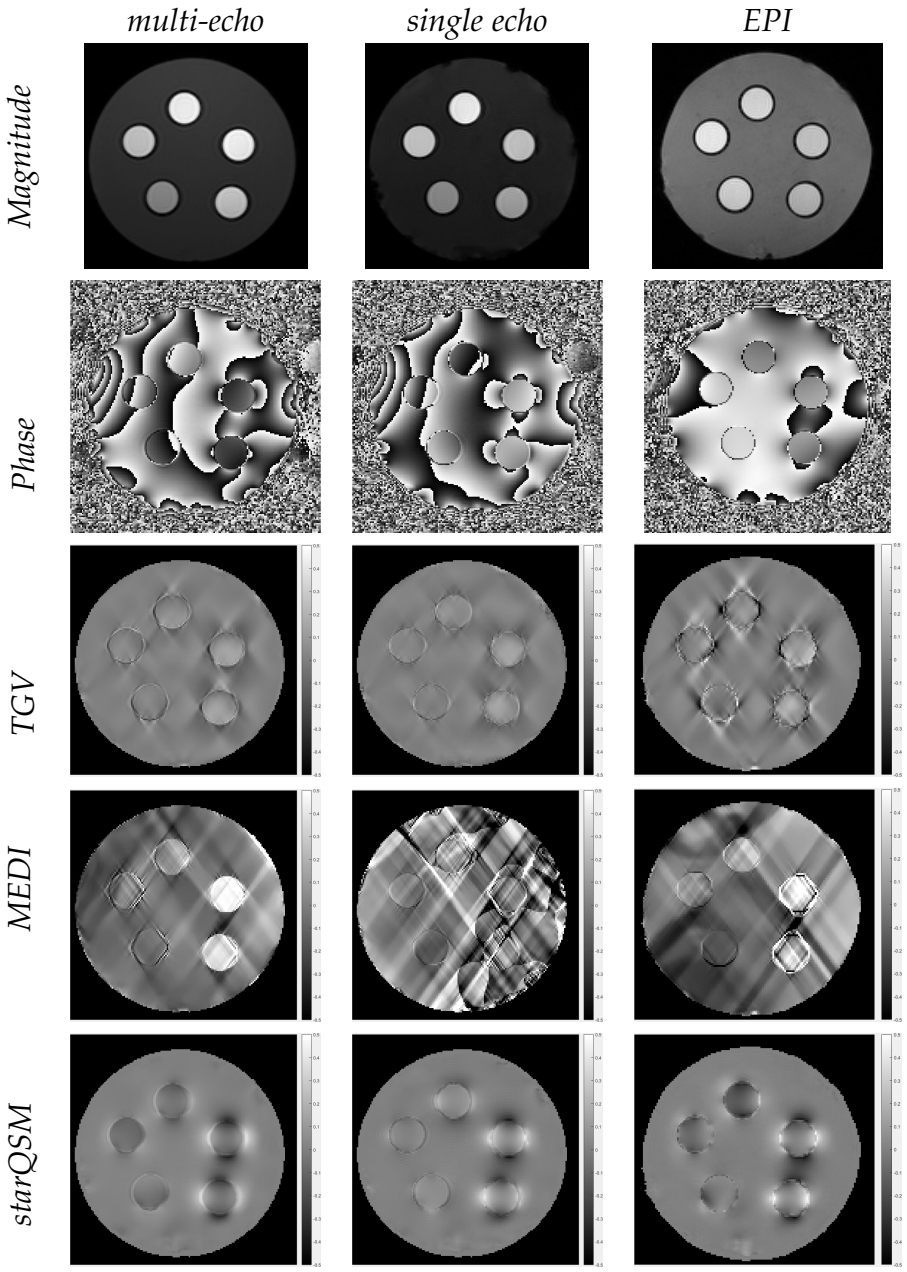

Figure 4.7: Magnitude images and quantitative susceptibility maps from phantom acquisitions for different sequences, susceptibility values range from -0.5ppm to 0.5ppm.

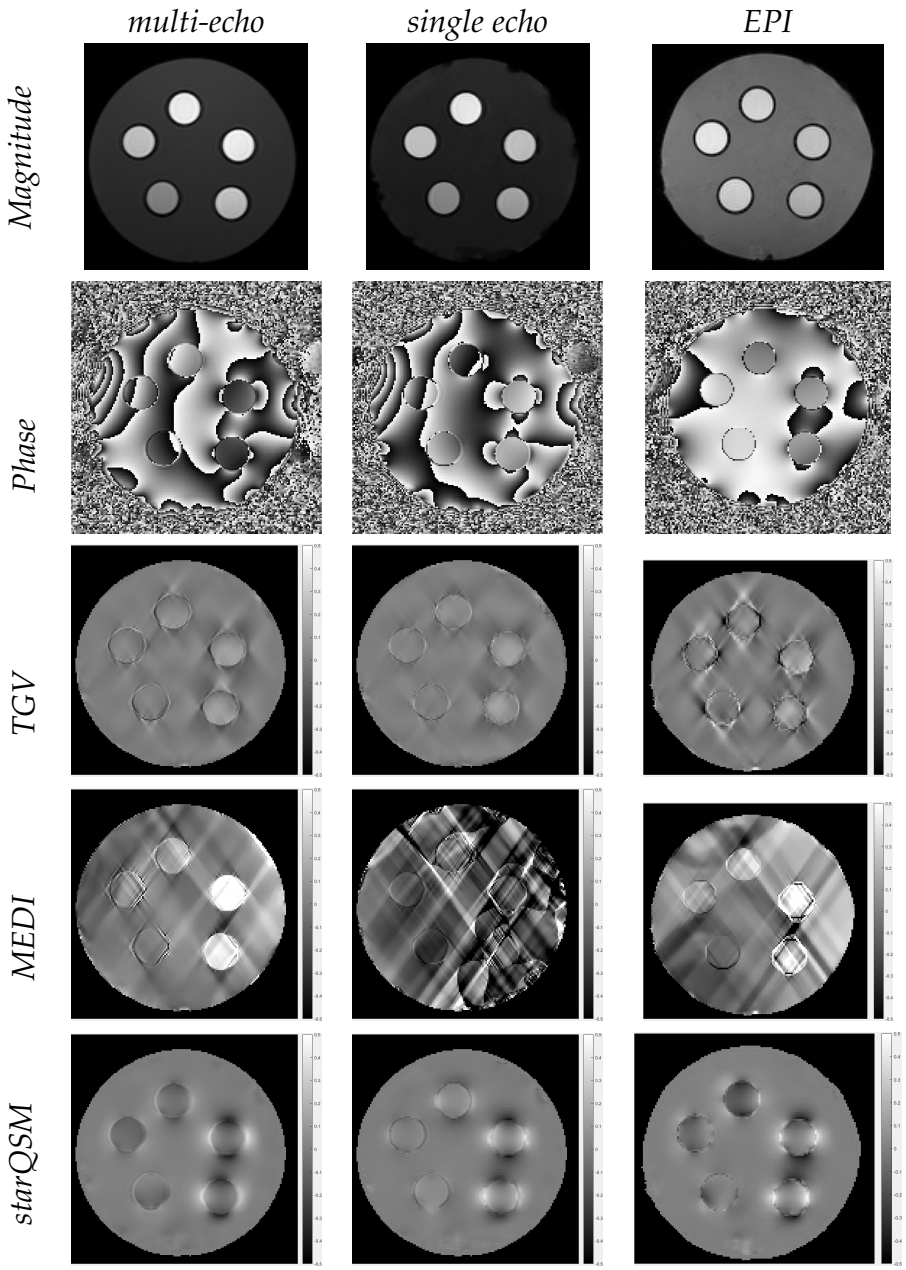

Figure 4.8: Magnitude images and quantitative susceptibility maps from phantom acquisitions for different sequences, normalized voxel values, susceptibility values range from -0.5ppm to 0.5ppm.

4.3.2 Accuracy of susceptibility in phantom vials

The plots in Figure 4.9 show the evaluated susceptibility values over their corresponding underlying solution concentration (Table 4.1), normalized and noted as $\Delta\chi$. The calculated quantitative susceptibility values did not exactly correspond to the expected theoretical calculations of susceptibility values (given in Table 4.2), based on Magnevist® [47] concentrations and the molar susceptibility. All values are biased. Nevertheless, for TGV a linear relationship was determined between the calculated and expected susceptibility values. Noticeable in Figure 4.9 is that only the MEDI and TGV algorithms lead to r^2 values greater than 0.7. The resulting linear equations for the TGV algorithm are displayed in Figure 4.10 (calculated with unreferenced results). The relative error for the TGV algorithm in each phantom vial was calculated according to Equation 4.4 and is given in Table 4.3. With decreasing expected susceptibility, the relative error increases for the single echo and EPI sequence.

Sequence	expected susceptibility (ppm)	calculated susceptibility (ppm)	relative error (%)
multi-echo	0.815	0.124	84.77
	0.401	0.054	86.43
	0.205	0.028	86.11
	0.101	0.016	84.14
single echo	0.815	0.131	83.91
	0.401	0.036	91.02
	0.205	0.018	91.04
	0.101	-0.003	103.01
EPI	0.815	0.143	82.48
	0.401	0.078	80.55
	0.205	0.018	91.32
	0,101	-0,02329	123.06

Table 4.3: Phantom expected and calculated susceptibility values (TGV algorithm) with corresponding relative error.

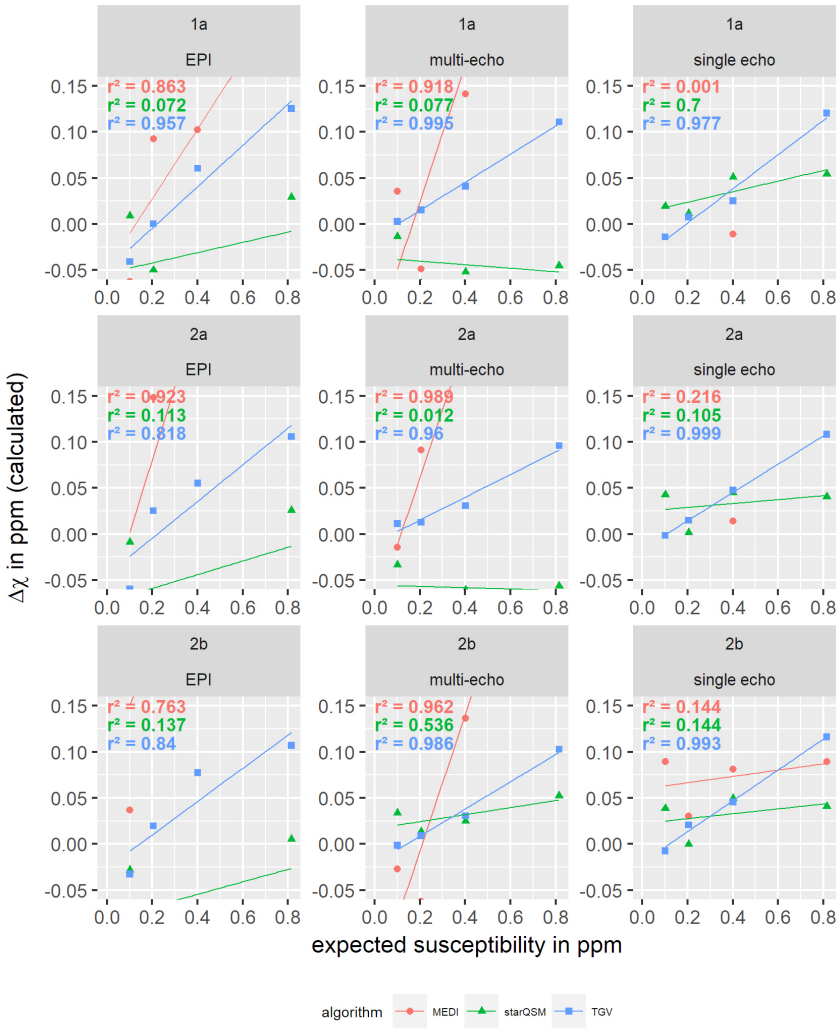

Figure 4.9: Phantom expected over calculated susceptibility values with r^2.

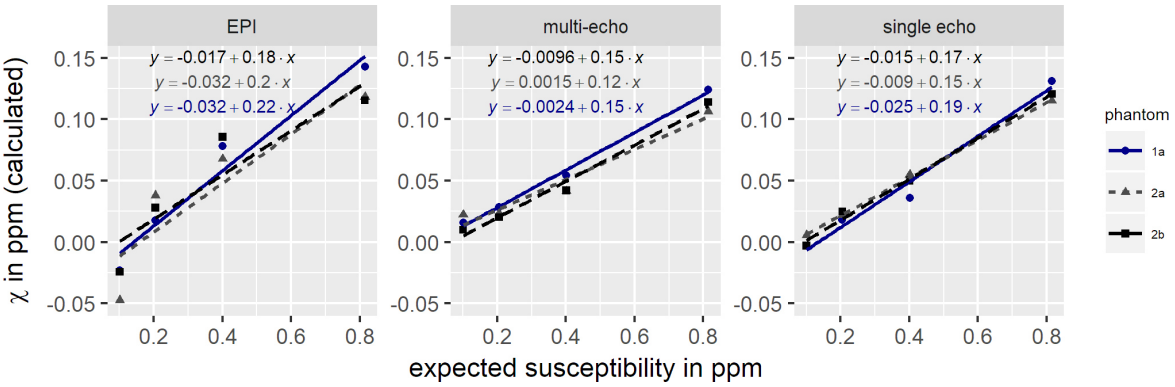

Figure 4.10: Phantom measurements with corresponding equations, TGV algorithm.

4.3.3 Repeatability and Reproducibility in phantom experiments

For evaluation of the repeatability and reproducibility the whole phantom was measured three times (1a, 2a, 2b). The resulting relative standard deviations (RSDs) can be found in Table 4.4. Overall the RSDs are quite high, especially for smaller susceptibility values and for EPI data. The results of the single and multi-echo GRE on the other hand are more reasonable and in the same range. As summarized in Tables 4.5 and 4.6, there was no significant difference between the two measurements regarding repeatability and reproducibility. Also the Bland-Altman plots in Figures 4.11 and 4.12 show that for the multi-echo and single echo sequence all values are in the 95% limits of agreement.

Sequence	χ in ppm	Repeatability RSD%	Reproducibility RSD%
EPI	**0.101**	70.61	87.52
	0.205	68.67	80.67
	0.401	27.15	21.09
	0.815	17.13	18.63
multi-echo	**0.101**	17.86	48.51
	0.205	19.02	24.44
	0.401	21.68	25.46
	0.815	7.66	8.63
single echo	**0.101**	24.56	55.05
	0.205	20.56	20.38
	0.401	31.18	19.34
	0.815	6.24	6.24

Table 4.4: Relative standard deviations of reproducibility and repeatability for the TGV algorithm calculated by equation 4.2.

	Ho	p value	Interpretation (p>0.05)
EPI	no significant difference	0.439	there is no significant difference between the two measurements
multi echo	no significant difference	0.676	there is no significant difference between the two measurements
single echo	no significant difference	0.739	there is no significant difference between the two measurements

Table 4.5: Summary of Welch t-test results regarding the repeatability measurements, TGV algorithm.

	Ho	p value	Interpretation (p>0.05)
EPI	no significant difference	0.426	there is no significant difference between the two measurements
multi echo	no significant difference	0.259	there is no significant difference between the two measurements
single echo	no significant difference	0.6409	there is no significant difference between the two measurements

Table 4.6: Summary of Welch t-test results regarding the reproducibility measurements, TGV algorithm.

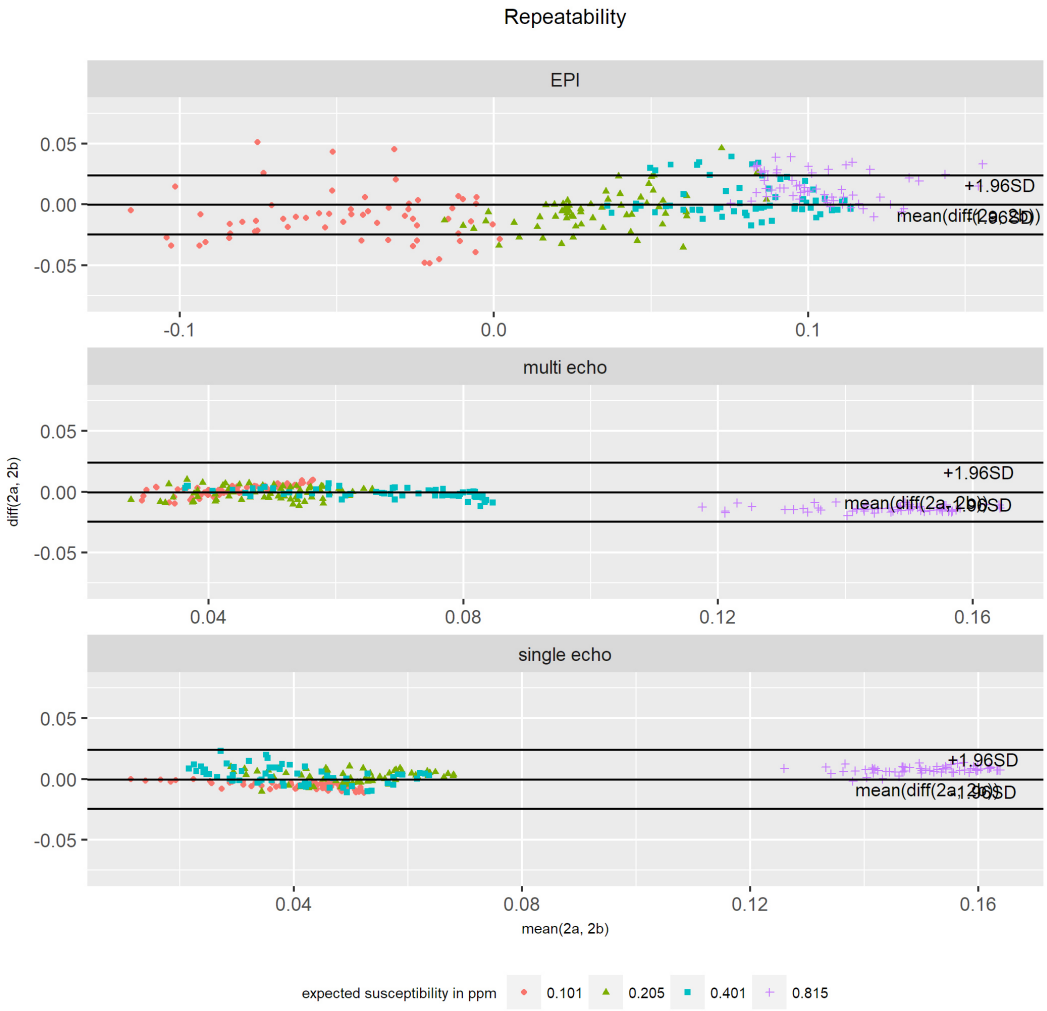

Figure 4.11: Bland-Altman plot for repeatability.

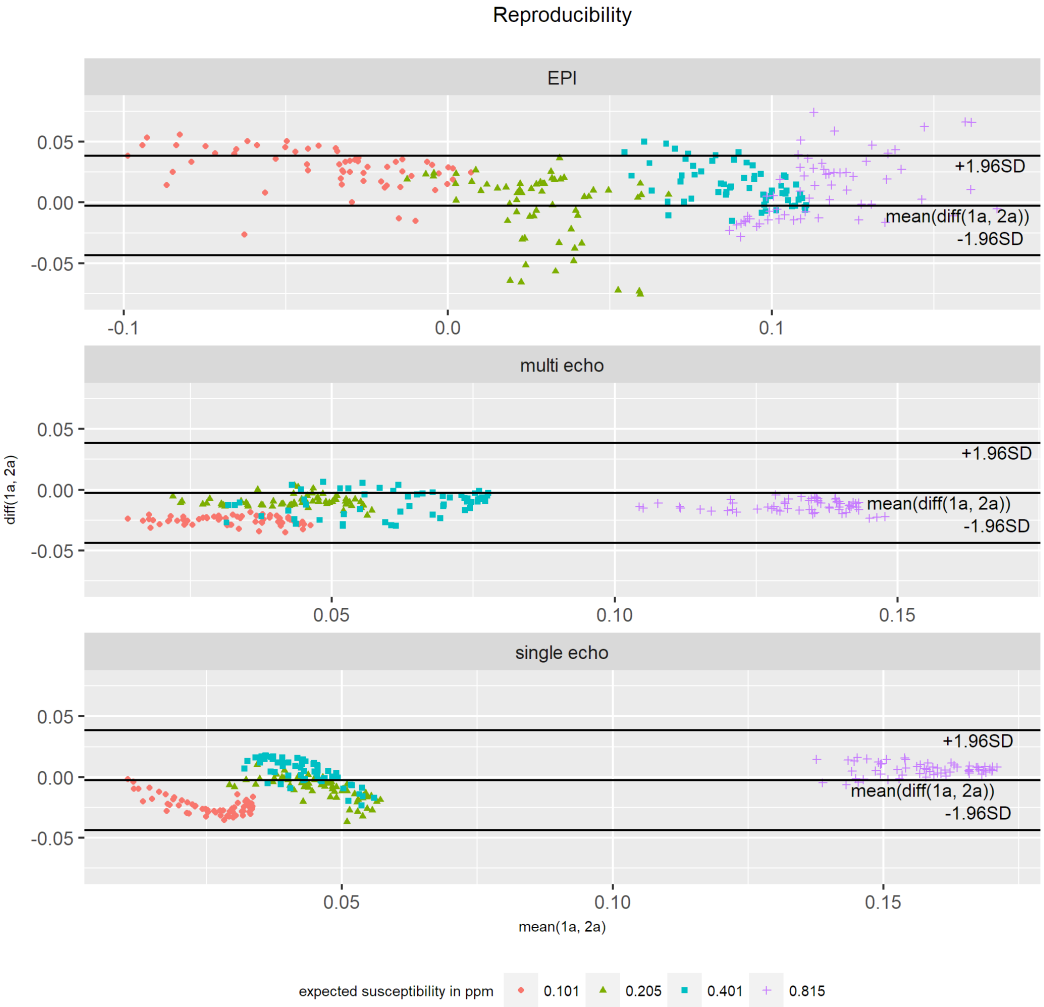

Figure 4.12: Bland-Altman plot for reproducibility.

4.3.4 QSM algorithm precision in ex situ porcine hearts

Regarding the ex situ porcine heart measurements, Figures 4.13, 4.14, 4.15, 4.16 and 4.17 show the mean susceptibility values with their corresponding standard error for three ROIs in each of the five hearts. These correspond to the labels given in Figure 4.4. Due to the fact, that the real susceptibility values are unknown, the measurements of ex situ porcine hearts only determines the precision of the algorithm. No statements can be made regarding the accuracy of the algorithms. In terms of precision, the TGV algorithm provided the best result.

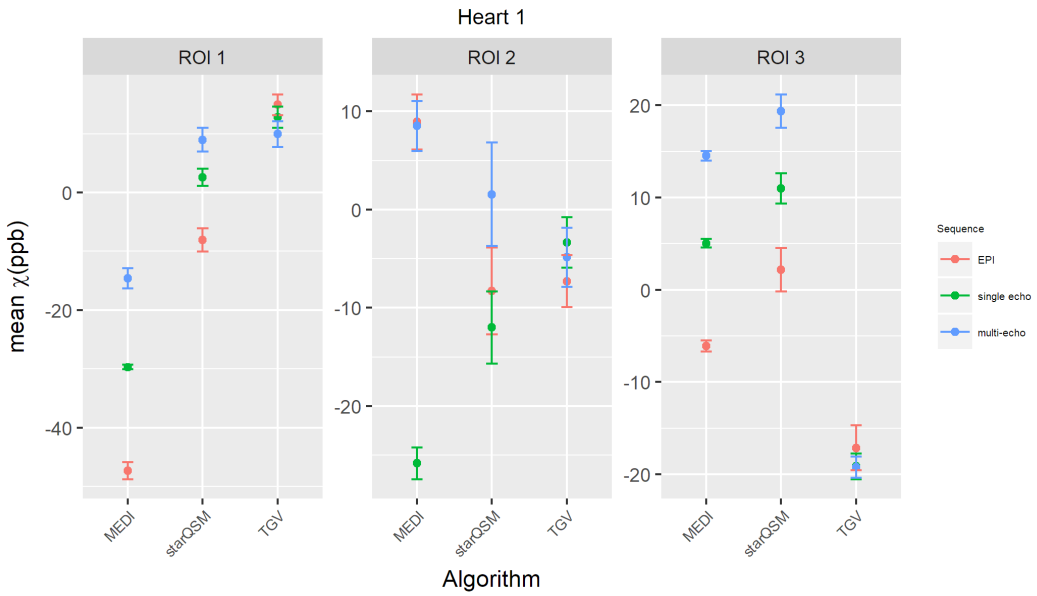

Figure 4.13: Mean susceptibility values heart and standard error, heart 1.

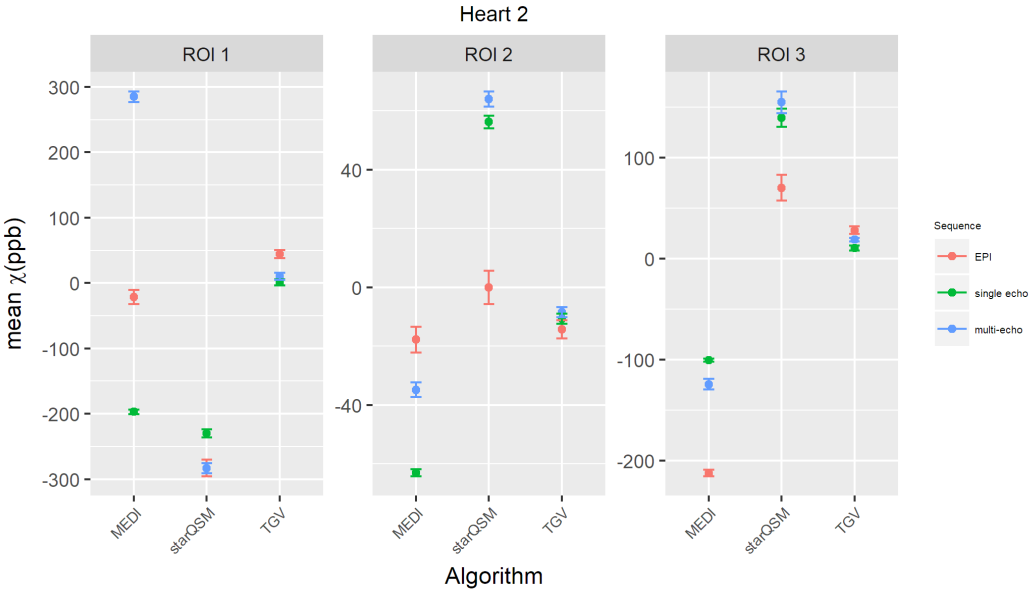

Figure 4.14: Mean susceptibility values and standard error, heart 2.

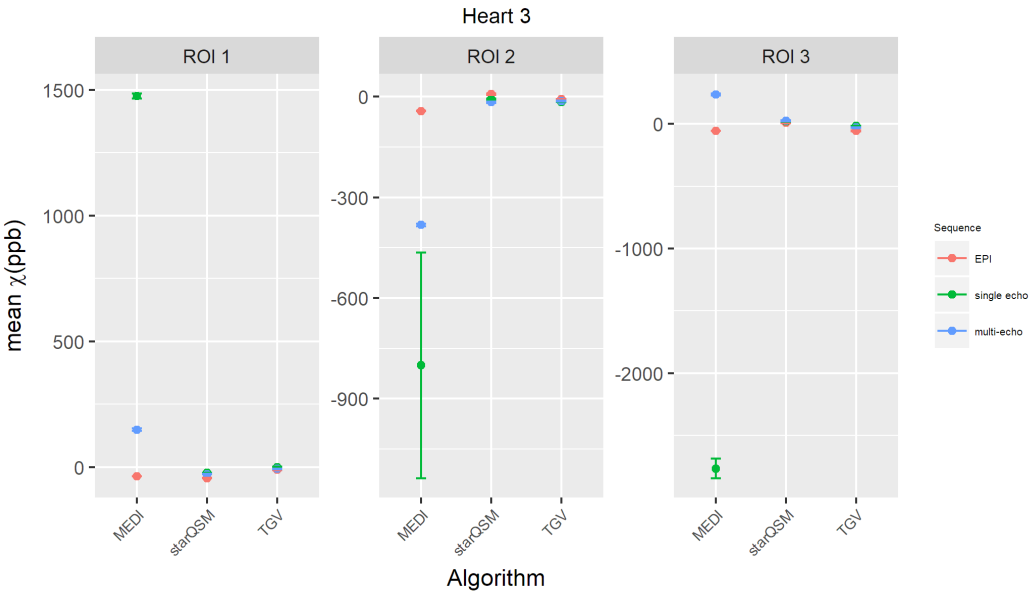

Figure 4.15: Mean susceptibility values and standard error, heart 3.

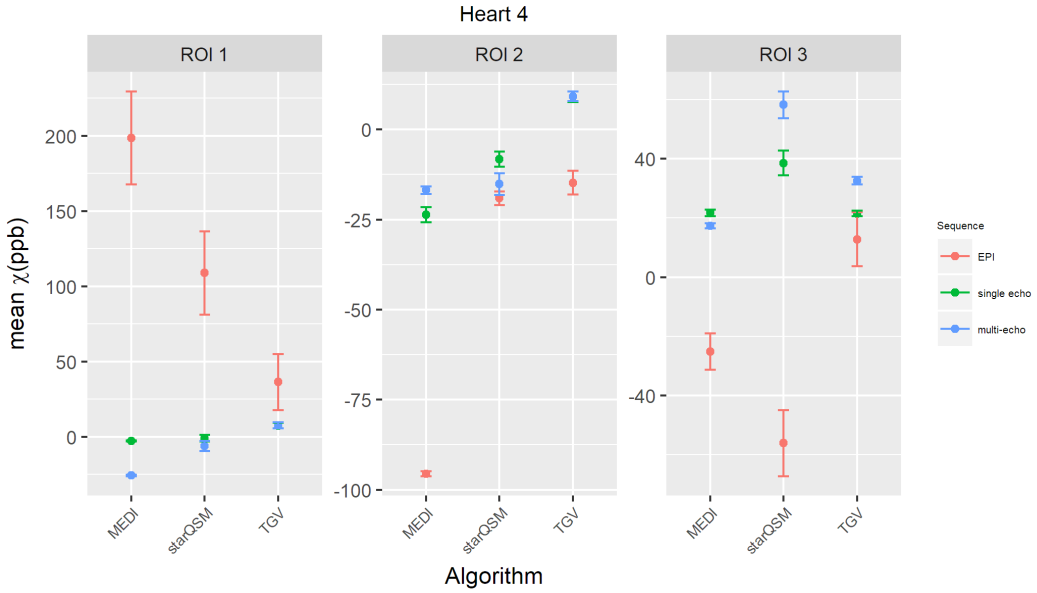

Figure 4.16: Mean susceptibility values and standard error, heart 4.

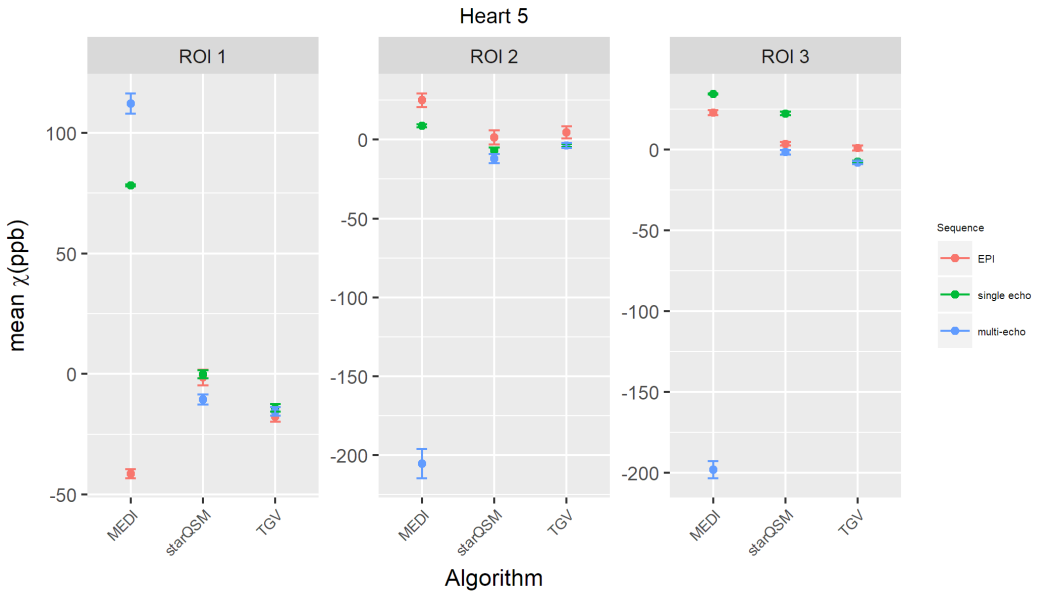

Figure 4.17: Mean susceptibility values and standard error, heart 5.

To gain information about the influence of the input sequence, an evaluation with violinplots, seen in Figures 4.18 and 4.19, showing the susceptibility values for all voxels in the given ROI, was made. The boxplots in the center of the violinplots indicate the median and the upper and lower quartile of the specific ROI. Table 4.7 gives a summary of the Welch t-test results. Each group consists of nine ROIs where all sequences were compared with one another in a pairwise manner to test for significant differences. In water, the occurrence of significant differences was reduced. Overall, there were less ROIs with a significant difference between the sequences when the embedding media was water, instead of air. Figure 4.22 shows the myocardium quantitative susceptibility maps of the three algorithms. The plots in Figures 4.20 and 4.21 show the confidence intervals calculated by the Tukey's test, indicating significant differences when the confidence interval does not contain zero. For the ANOVA a confidence level is 95% was used, which corresponds to a significance level of 0.05.

	Significant difference in ROIs with $\alpha = 0.05$		
	multi-echo/single echo	**EPI/multi-echo**	**EPI/single echo**
Air	6 out of 9	8 out of 9	6 out of 9
Water	3 out of 9	5 out of 9	3 out of 9

Table 4.7: Summary of significant differences in the evaluated ROIs.

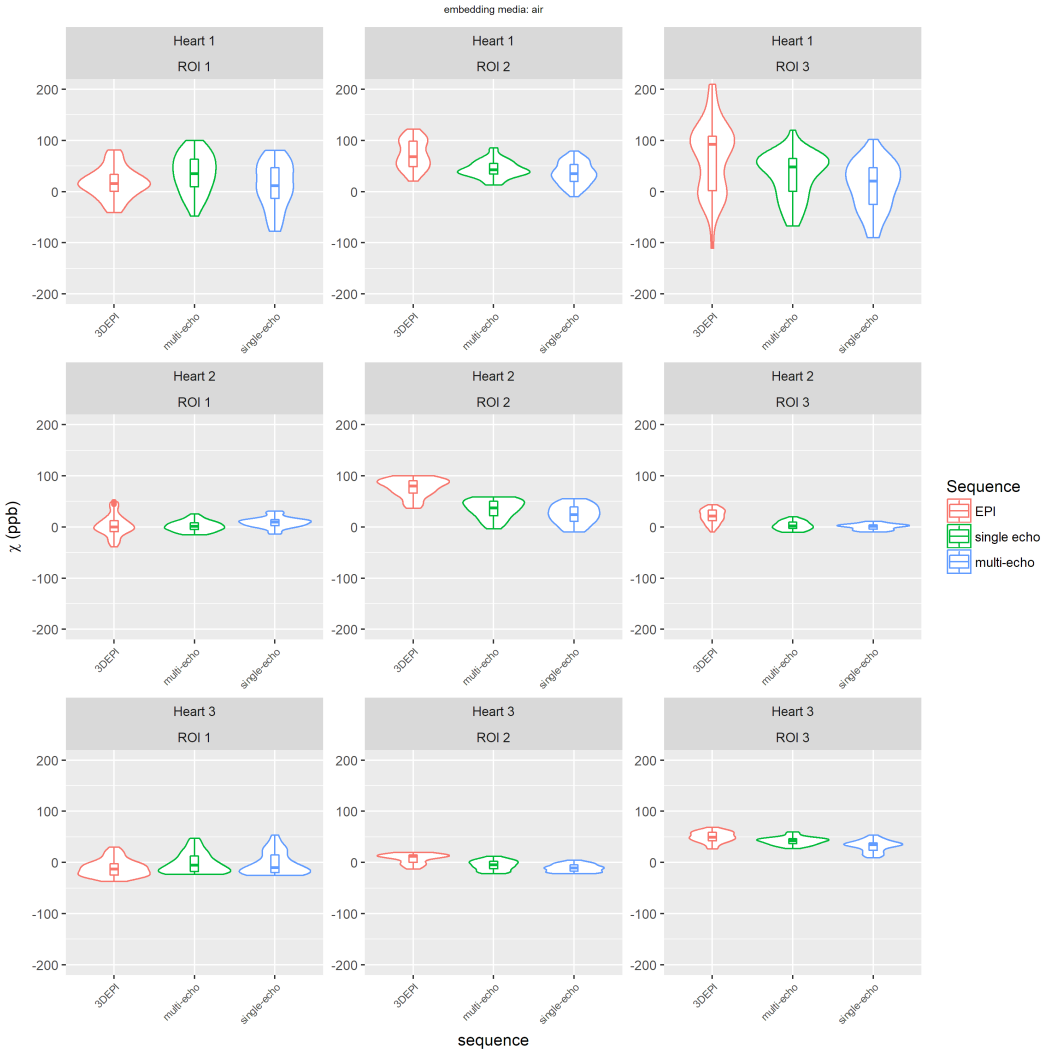

Figure 4.18: Susceptibility values for hearts embedded in air, TGV algorithm.

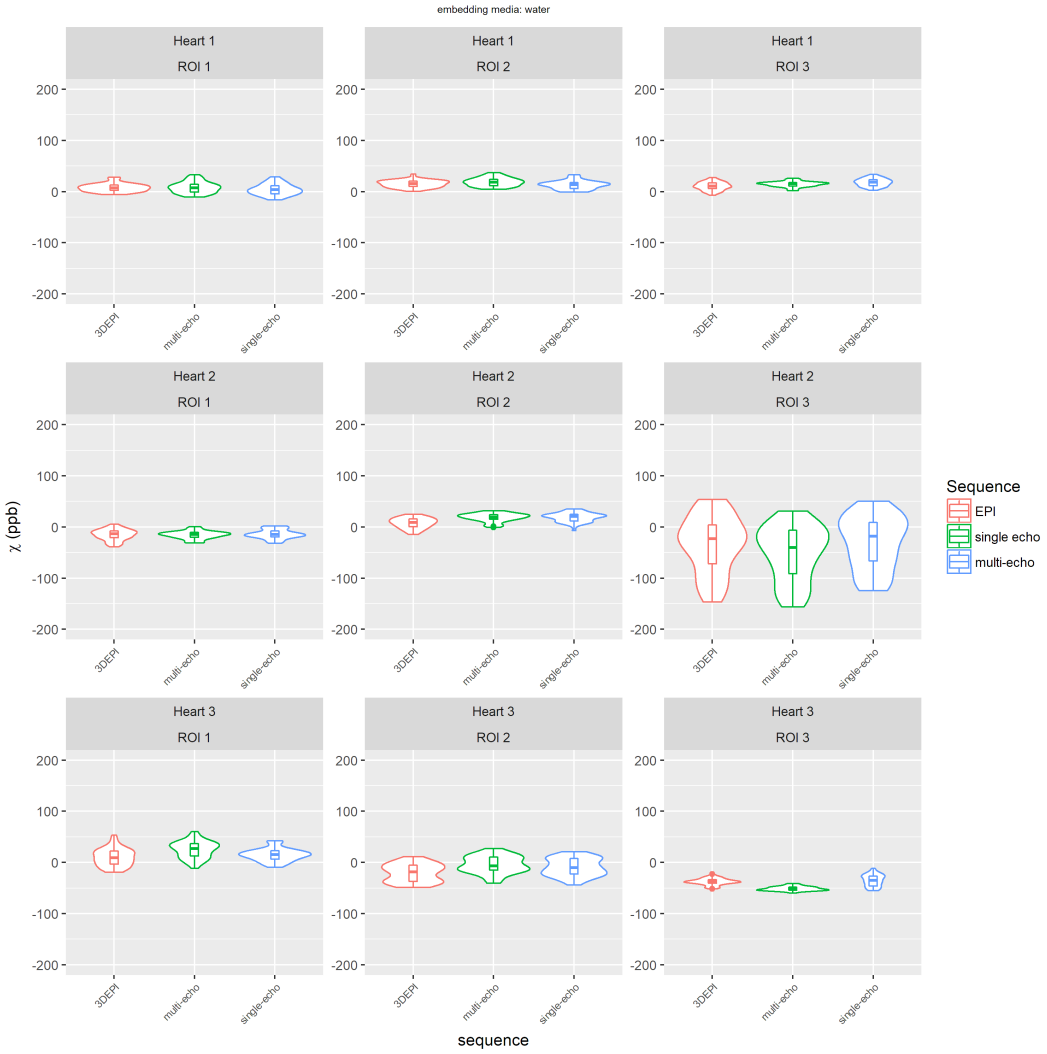

Figure 4.19: Susceptibility values for hearts embedded in water, TGV algorithm.

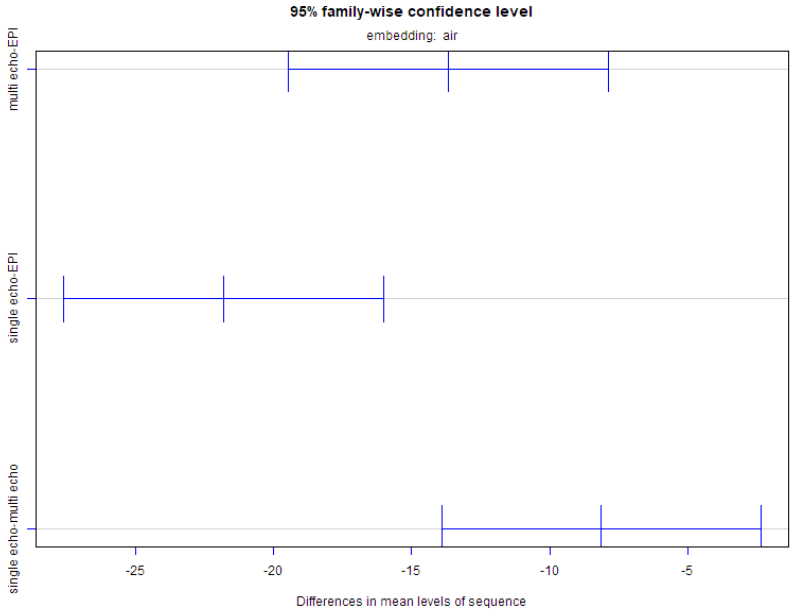

Figure 4.20: Confidence interval Tukey's test, embedding media: air, TGV algorithm.

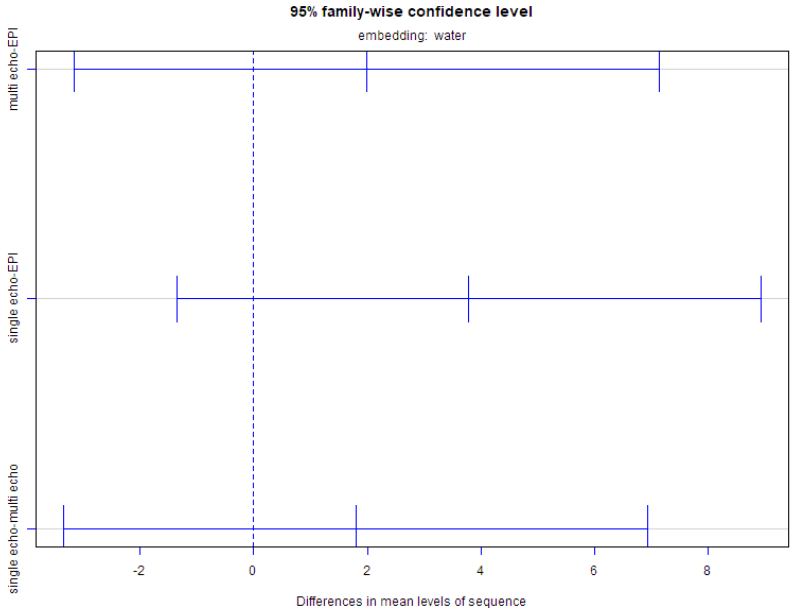

Figure 4.21: Confidence interval Tukey's test, embedding media: water, TGV algorithm.

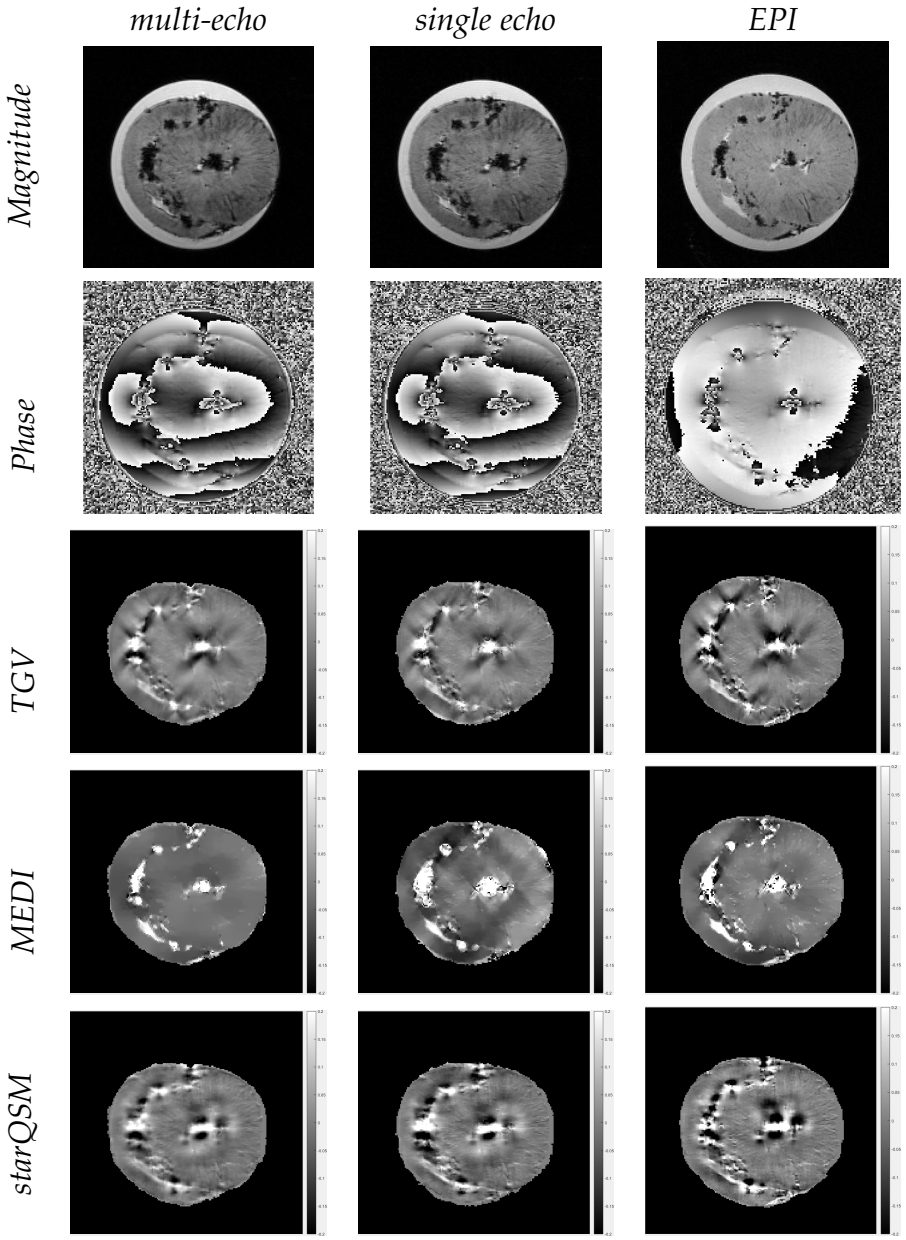

Figure 4.22: Magnitude and QSM images of an ex-situ porcine heart, coronal slice 24, acquisitions for different sequences, susceptibility values range from -0.2ppm to 0.2ppm.

4.4 Discussion

4.4.1 Image Quality in phantom experiments

Regarding SNR, the multi-echo sequence resulted in to the lowest values with the sequence parameters given in Table 3.1.

Between the EPI and single echo GRE sequences the SNR is in the same range. In general, the highest signal is given at the Ernst-angle, denoted in Equation 4.5 [51].

$$\alpha = arccos(e^{-TR/T1}) \tag{4.5}$$

In ex situ porcine hearts, T1 is approximately 720ms [35]. The flip angles used for multi-echo and single echo GRE agree with the Ernst-angle, whereas the flip angle of the EPI sequence was set suboptimal below the Ernst-angle . However, as the lower flip angle results in less signal, the flip angle parameter of the EPI can be improved.

The smaller SNR values of single and multi-echo GRE compared to the EPI sequence could be due to the lower in plane resolution, resulting in smaller voxels and therefore less signal in each voxel summing up into a lower overall signal and so SNR decreases.

To use the sequence as an input for QSM a high SNR and a high image resolution must be ensured [52]. Since there are no big differences between the given sequences, all three would be considered.

The phantom measurements should serve as a basis for an algorithm evaluation in terms of precision, accuracy, reproducibility and repeatability. The gradation of the gray values from lighter (higher susceptibility values) to darker (lower susceptibility values) corresponds to the underlying relation (Table 4.1). All images were scaled from $-0.5ppm$ to $0.5ppm$. A difference in gray values can be seen best in the vials of the TGV algorithm, which matches with the liner relation when evaluating the ROIs (Figure 4.9). In general, all QSM images showed artifacts around the vials, however, the images of the MEDI algorithm leaded to severe streaking artifacts (Figure

4.8). The TGV algorithm shows local streaking artifacts at local air bubbles in the agarose surrounding embedded vials. These effects were stronger when using the EPI sequence instead of the multi-echo or single echo GRE. The fewest streaking artifacts are found when using the starQSM algorithm, but a systematic artifact can be found at the vials border, stronger at vials containing the higher concentrations. In all algorithms image quality does not change when the values are normalized (see Figures 4.7 and 4.8). The center, consisting of 1.7% agarose gel should have an underlying susceptibility of nearly water, which is $-9,035ppm$ [53, 54]. As a result, the vials containing paramagnetic substances, should have gray values lighter than the center of the phantom, which is not given at the starQSM images. This reflects the poorer performance of this algorithm to accurately reconstruct the quantitative susceptibility values for each pixel. Due to this inferior performance of the MEDI and starQSM algorithm, the following evaluations and calculations were only done with the TGV algorithm.

As the vial borders show susceptibility artifacts in all algorithms, one improvement could be embedding the solutions in a container with a thinner wall thickness, for example thinner than the voxelsize of the sequence to reduce artifacts at the borders. In the work by Wei et al. [30] balloons with a wall thickness of 100μm were used, which resulted in reduction of susceptibility effects of the balloons.

4.4.2 Accuracy in phantom experiments

All three algorithms did not lead to the correct underlying values, which should be in range of $0,101ppm$ to $0,815ppm$ (Table 4.1). However, TGV algorithm showed a linear relation of the susceptibility values to the underlying Magnevist solution in all measurements and in almost all measurements the MEDI algorithm (Figure 4.9), meaning that the the ratio of the underlying values is correct, but the results are biased. There was no linear relationship found in the starQSM algorithm, which could be due to a stronger sensitivity to acquisition noise which influences the susceptibility map calculations [55]. In the presence of localized air bubbles, starQSM demonstrated less streaking artifacts compared with MEDI and TGV algorithms, which severely suffered in the presence of such bubbles.

The relative errors for the TGV algorithms given in Table 4.3 vary for the EPI and single echo sequence with decreasing expected susceptibility. The values are in the same range for the mutli-echo sequence. As all calculated susceptibility values are biased to the expected underlying susceptibility values, the relative error should stay the same for varying susceptibility values. Apart from the bias, this would indicate that the multi-echo sequence provides the most reliable values.

Although the TGV results were biased, the algorithm showed a good reproducibility and repeatability (see Figures 4.11 & 4.12 and Tables 4.5 and 4.6). The Welch t-test showed that there were no significant differences between the measurements, leading to the classification of TGV as a stable and robust algorithm with a good repeatability and reproducibility.

In a recent study by Olsson et. al [46] the effects of cylinders with varying angles relative to $B0$ on the calculated susceptibility values with the MEDI algorithm were investigated. When the angle was close to the magic angle or larger, the calculated susceptibility values were biased. Further, with an non parallel orientation of the cylinders to $B0$ blooming effects appeared. Overall, this confirms the findings in the present acquisitions where the phantom was orthogonally aligned to $B0$ resulting in biased susceptibility values, but correct findings in the underlying linear relation.

According to literature each algorithm was tested on accuracy and image quality using a numerical phantom for the TGV algorithm and a real phantom for the MEDI and starQSM algorithm.

In a study by Tian Liu et. al [55] the MEDI algorithms accuracy was determined on both, a numerical and a real phantom. For the investigation, a numerical phantom with a sphere, a shell and a cylinder mimicking common structures was used. To evaluate the influence of noise, ten different numerical phantoms with different noise levels were taken into account. The physical phantom consisted of a 2% agarose gel containing five balloons with gadolinium solution with known susceptibility values and was scanned with a multi-echo gradient echo sequence. One of the results was that the reconstruction error correlated linearly with the acquisition noise. Furthermore, the quantitative susceptibility maps contained severe streaking artifacts which are dependent on the quality of the spatial prior. With increasing quality of the gradient image, the streaking artifacts were found

to diminish. All in all it can be stated that the MEDI algorithm leads to a unique solution when no acquisition noise present and when a perfect spatial prior is given [55]. Olsson et. al found out that varying background field removal methods and the choice of the regularization parameter λ is not affecting the quantitative result a lot [46].

The starQSM algorithm's accuracy was tested on a phantom with known susceptibility values. The cylindrical phantom consisted of gadolinium solutions with a concentration of 0.25%, 0.5% 1% and 2% with corresponding susceptibility values of 0.4, 0.81, 1.63 and 3.26ppm (room temperature), filled in long latex balloons embedded in a water container. The image acquisition was done with a multi-echo 3D spoiled-gradient-recalled sequence. The results were standard errors of 6%, 2.5%, 3% and 6%. Streaking artifacts and quantification errors can originate from strong susceptibility sources and by noise amplification when solving the ill-posed inverse problem. Another reason for streaking artifacts can be imperfectly unwrapped phase and residual background phase. Currently, a complete artifact absence is not possible which would need improvement of current QSM processing to a more robust technique using high resolution input data with minimized noise [30].

The TGV algorithm was tested on a numerical phantom (adapted from [56]) which was created by an automated segmentation of brain regions into white matter, gray matter and cerebrospinal fluid resulting in a phantom with values similar to in vivo. To make the phantom more realistic, air-tissue interfaces were mimicked with focal susceptibility perturbers and two random susceptibility sources were added outside of the brain. The final phantom was then convolved with the dipole kernel followed by phase wrapping from $-\pi$ to π. As a last step white noise was added to the phase data. At the end a brain mask was used. The algorithm evaluation of the phantom has proved the superiority of the TGV algorithm compared with the TV reconstruction. Where the TV based reconstruction yielded to staircasing artifacts but the TGV reconstruction to smoother results although structural borders are retained [32].

4.4.3 Repeatability and Reproducibility in phantom experiments

Regarding repeatability and reproducibility, in all three sequences there were no significant differences between the measurements (Tables 4.5 and 4.6), but when looking at the relative standard deviations (Table 4.4), the values are quite high. This result is considered to originate from the overall high standard deviation in the susceptibility ROIs. While the GRE sequences resulted in a similar range of RSD, the RSD in susceptibility maps calculated from EPI data were consistently higher. The RSDs were higher when the measured susceptibility values were smaller, as acquisition errors have a higher weight on the smaller susceptibility values.

Assuming susceptibility values in the myocardium around $-30ppb$ and $30ppb$, presented in the work by Dibb et. al. [57] in an excised mouse heart myocardium, then the RSD for single and multi-echo GRE would be around 20% for repeatability and 50% for reproducibility. These are the RSD values given in Table 4.4, which correspond to the lowest susceptibility of 101ppb. With values of up to 70% and 87% for repeatability and reproducibility using the EPI sequence, it becomes clear that the EPI differs a lot from the other to sequences, which indicates that it is not suitable as a reliable sequence for QSM.

The Bland-Altman plots demonstrate unbiased results for the multi-echo and single echo phantom measurements, as all values are in the 95% limits of agreement (Figures 4.11 and 4.12). A trend can be found in the multi-echo and single echo data. The difference between the two measurements (ordinate) for the single echo data decreases when the susceptibility are higher. The opposite trend can be found in the multi-echo data. This leads to the assumption that the repeatability decreases when the underlying susceptibility values are higher.

4.4.4 QSM algorithm precision in ex situ porcine hearts

Overall, in terms of precision the TGV algorithm performed best for the ex situ hearts. For all given regions the resulting magnetic susceptibility

property, diamagnetic or paramagnetic tissue, was the same for all hearts and regions. The variation of values could be due to local sources of air nearby which may have influenced the acquisition sequences and algorithms. Slight movements of the heart during the measurements in the water may also have caused a redistribution of water and therefore air within the container. This would of course affect the local magnetic susceptibility due to local air bubbles.

In Figure 4.22 quantitative susceptibility maps of an ex situ porcine heart calculated by the three different algorithms for each input sequence are shown. As already mentioned earlier, the MEDI algorithm showed the most streaking artifacts, which are demonstrated in the myocardium images, especially for the single echo sequence. A similarity between artifacts at tissue borders can also be found with the phantom, where border artifacts are in round shapes for the starQSM algorithms images and have a striped shape for the TGV algorithm. The comparison shows, how the different algorithms handle local air regions, where in all three the air sources do not have a well defined border to the adjacent myocardium. Comparing the susceptibility maps to magnitude images, the starQSM and TGV algorithm show much more details than the MEDI algorithm, which shows no delineation of small myocardium structures. Regarding small structures in the myocardium the TGV and starQSM algorithms led to the same results, but both suffered from artifacts near sources of air or fluids located in the myocardium.

The reconstruction algorithms and their robustness with various acquisition strategies were evaluated based on the observed standard error. When looking at the error bar plots in Figures 4.13, 4.14, 4.15, 4.16 and 4.17 it is obvious that there is a huge difference between the algorithms and their accordance of the different sequences. Overall, in the evaluated ROIs the MEDI and starQSM have larger standard errors than the TGV, where in most cases the EPI sequence values are higher than with single or multi-echo. When looking at the magnitude images of the hearts, they all show a different structure of the myocardium with a different amount of air and fluids embedded.

The intervariability is higher at hearts 2, 3 and 4. Reasons may be found in the underlying magnitude images which display different sources of air in the tissue. The myocardium in hearts 1 and 5 show a more homogeneous

myocardium structure than the others, seen on the magnitude images in Figure 4.23.

Comparing the three latest algorithms, similar susceptibility values for different sequences with the TGV algorithm indicates that it is the most robust algorithm independent of the input sequence. For the starQSM and the MEDI algorithm the resulting susceptibility values were dependent on the measured sequence. As a result, these two algorithms were not included in any further evaluations, where only the TGV algorithm was used.

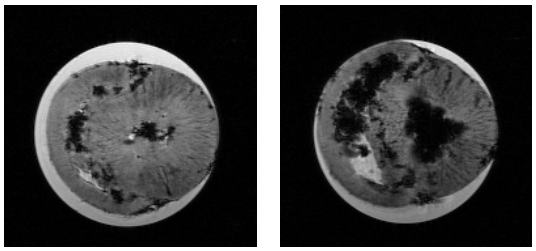

(a) Heart 1

(b) Heart 2

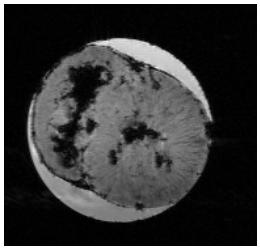

(c) Heart 3

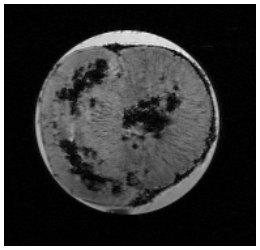

(d) Heart 4

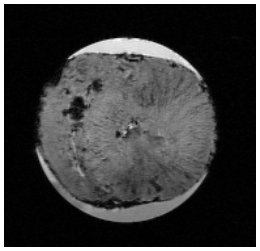

(e) Heart 5

Figure 4.23: Porcine hearts, single echo, magnitude images, slice 24.

Using TGV reconstruction, the sequence evaluation showed good agreement between three sequences (Figures 4.18 and 4.19). The distribution of the

susceptibility values in the selected ROIs agree better where the embedding media is water instead of air. Noticeably the EPI often had different distributions than those of single echo and multi-echo GRE data. A reason for the difference of the EPI sequence to the single echo and multi-echo GRE could be that echo-planar imaging based sequences are more sensitive to magnetic field inhomogeneities, which can lead to pixel shifts in the phase encoding direction [58]. The usage of less RF refocusing pulses in echo-planar imaging than in conventional gradient recalled echoes sequences, results in an aggregation of a phase error in phase-encoding direction. Using external coils for shimming often does not compensate the high order magnetic field inhomogeneities [58, 59]. As EPI often uses long acquisition trajectories with a T2* signal decay, it is easier affected by magnetic field inhomogeneities, which can lead to signal loss, image blurring and geometric distortions [60].

The increased occurrence of significant differences (Welch t-test, Table 4.7) between the three sequences used are stronger when the embedding media is air, compared to water, indicating that the water as embedding media is more suitable for a stable measurement independent of the input sequence. Further, the significant differences in water are less between the EPI and single echo GRE measurements than within the EPI and multi-echo measurements. The significant differences of quantitative susceptibility maps based on different acquisition sequences was also tested with the Tukey's test, a post-hoc test for ANOVA (Figures 4.20 and 4.21). As the confidence intervals are all containing zero when the embedding media is water, there is no significant difference between the quantitative susceptibility maps based on different sequences. In contrast, as the confidence intervals do not contain zero when the embedding media is air, reveal the significant difference in the susceptibility maps when different sequences are used. All in all, the experiments results suggests that there is an influence of the embedding media on the calculated susceptibility values. Therefore a further experiment was done with hearts in different embedding medias.

There was good agreement between the multi-echo and single echo GRE sequences. To optimize the experimental procedures for examinations in multiple media, only the EPI and multi-echo GRE were used for further data acquisitions (Chapter 5).

5 Hearts in different embedding media

5.1 Introduction

The final experiments were dedicated to gain information about the effect of different embedding medias on the magnetic susceptibility in the myocardium. As known, formaldehyde for example shortens $T2$ and $T2^*$ relaxation times, which means that quantitative MRI may be dependent on the surrounding of the post-mortem tissue [61]. The object, a porcine heart, was scanned using four different embedding medias. The acquisitions were built on the results of the algorithm and sequence evaluation in Chapter 4.

5.2 Methods

To obtain information about the influence of the embedding media on susceptibility values in the myocardium, three hearts were measured in four surroundings. Each heart was measured in all four different embedding medias (Figure 5.1). To ensure a more practicable workflow, the hearts were placed in the embedding medias in the following order, air, water, galden and finally embedded in agarose. After embedding the heart in water and galden, the hearts were not washed out. The embedding medias were chosen in terms of simplicity of application and with the aim to minimize local air bubbles on the outside of the myocardium. Since the substance Galden® HT80 has a very high density, it was selected to suppress air [62]. Note the good separation of blood in Figure 5.1 when using galden. Due to the fact

that it provides no MRI signal the resulting images were easy to segment because of no visual embedding media. The segmentation of the hearts was done with the Active Contour Segmentation in ITK-Snap. As already mentioned in Section 4.4, the good agreement of multi-echo and single echo results, the measurements in Chapter 5 included only multi-echo GRE and EPI sequences with parameters given in Tables 3.1 and 3.3, where the single echo GRE sequence was omitted. As the substance galden is quite expensive (around 600€ per 5kg [63]) it was filtered again after the acquisitions by using a separating funnel. The agarose gel concentration was set to 1.7% with 13.6g of agarose solved in 800ml of tap water.

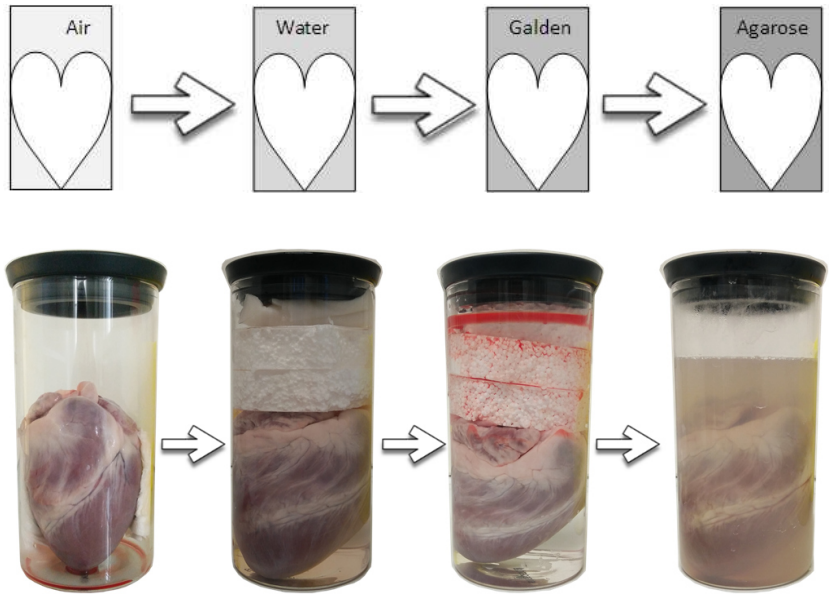

Figure 5.1: Porcine hearts in different embedding medias, workflow.

Due to a reorientation of the hearts when changing the embedding media, a 3D image registration for each of the three hearts was performed during post-processing. For this purpose the registration tool SimpleElastix was implemented in python [33]. For stable registration results, the image registration was done with the magnitude images and afterwards applied on the calculated quantitative susceptibility maps. As in previous experiments, the lack of a ground truth required alternative evaluation methods than comparison to the real underlying susceptibility. In this case, inspired by the work

of Dusek et al. [64], the comparison of the three hearts and their embeddings was done by calculating the z-score for each voxel in the specific ROI (Equation 5.1). The mean and the corresponding standard deviation used was calculated from all ROIs of all three hearts and embedding medias.

$$Z = \frac{X - \mu}{\sigma} \tag{5.1}$$

5.3 Results

In Figure 5.2 the boxplots of the z-scores for different embedding medias are given, showing a profound difference between the susceptibility values. There is a trend on the susceptibility values in the myocardium with respect to the embedding media. The highest susceptibility values are given in hearts embedded in agarose, followed by galden and water, where the air as surrounding media seems to have no systematic effect on the susceptibility compared to the others. Figure 5.3 shows the quantitative susceptibility maps of the myocardium, when the ex situ porcine heart was embedded in different substances.

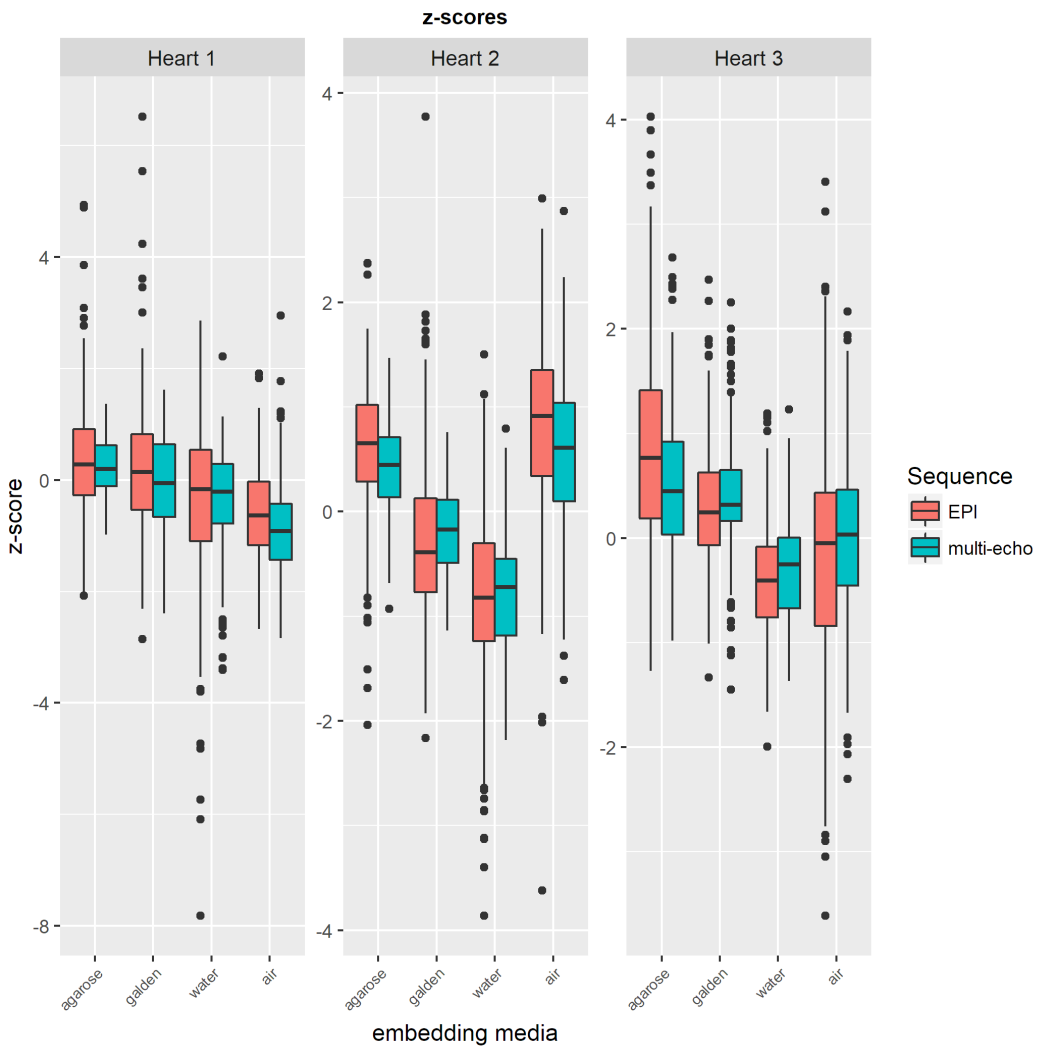

Figure 5.2: z-scores for three hearts in different embedding medias.

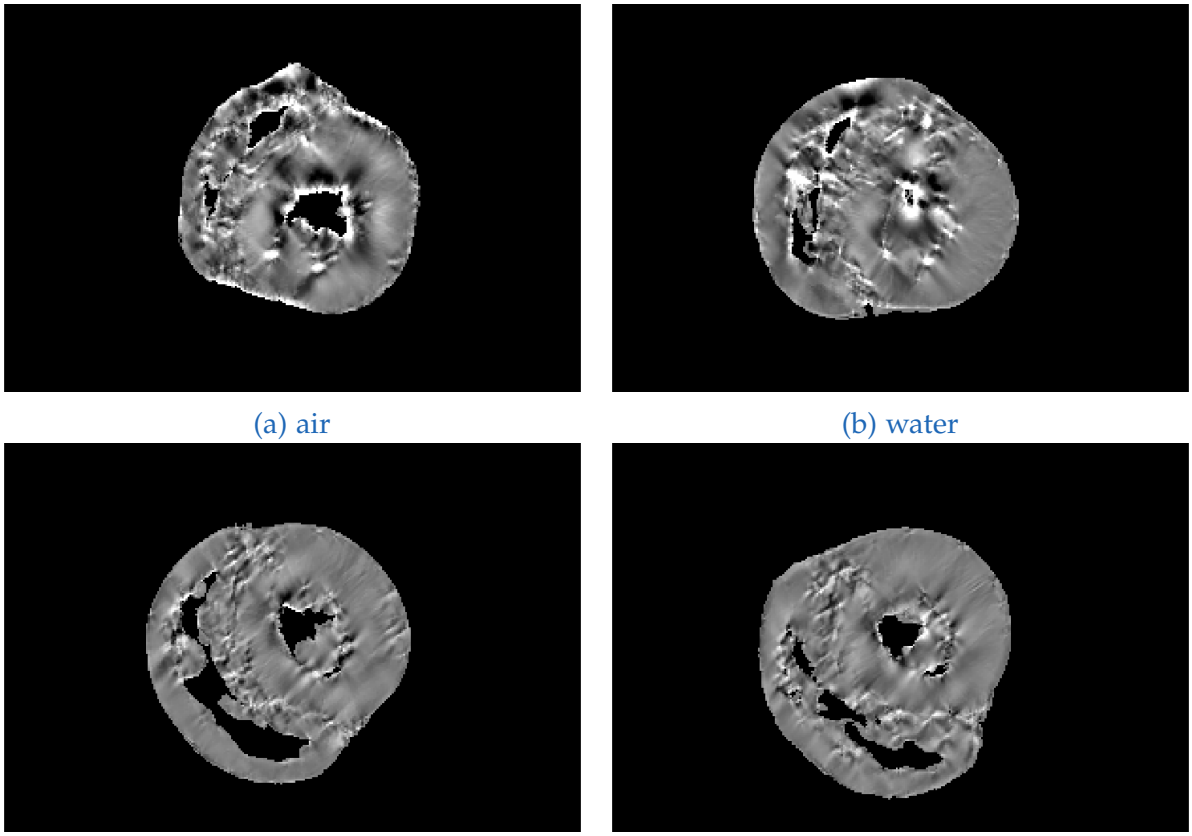

(a) air (b) water

(c) galden (d) agarose

Figure 5.3: QSM images in different embedding medias, TGV-algorithm.

5.4 Discussion

The z-score measures, how many standard deviations away from the mean a data point is. When calculating the z-scores, the distributions have a zero mean and a standard deviation of 1. With the z-scores the results can be compared to a "normal" population, which was in this case all hearts and all embedding medias. It expresses the deviation of values compared to a reference group [65, 66]. In medicine for example the z-score is used to express a patients bone density for the diagnosis of osteoporosis. A study by Burgkart et. al proved the feasibility of z-scores for quantitative analysis of osteoarthritis by MRI [67, 68].

The whole experiment was based on the assumption that the embedding media has an effect on the susceptibility values in the myocardium and therefore also on the quantitative susceptibility maps. Based on the plots in Figure 5.2 there is evidence that the embedding media affects the susceptibility values in the myocardium of ex situ porcine hearts. The highest susceptibility values are found with the embedding media agarose, followed by galden and water in decreasing order. No assumptions can be made about air, which led to lower values than water in heart 1, and in higher values than agarose in heart 2. However, additionally to the findings in Chapter 4, this confirms the assumption that air is not suitable as embedding media for quantitative susceptibility mapping of biological tissue, as it alters susceptibility values in a random manner.

In a experiment by Dusek et al. [64] the effect on different embeddings on the brain was investigated, where they found direct evidence that the medium surrounding the tissue has an effect on the QSM measurements. In contrast to their work, where the agarose had the strongest attenuating effects on the susceptibility values in the brain tissue, in this experiment the agarose showed the highest susceptibility values in the myocardium.

Further differences of the embeddings can be found in the quantitative susceptibility maps (Figure 5.3), especially at the border of the segmentations. When using galden or agarose surrounding the tissue, artifacts due to susceptibility jumps at the border of the myocardium are reduced. When using air as an embedding media (Figure 5.3a) strong artifacts are present

at vessel or air regions borders appearing as strong black borders. Comparing the quantitative susceptibility maps with the embeddings galden and agarose (Figures 5.3c and 5.3d), a few more details in the myocardium structure may be found with the embedding media galden. Another benefit of galden is the good delineation of the myocardium, as it provides no MR signal, resulting in an easy automated segmentation due to a good image contrast in the magnitude images. As air does unforeseen changes to the susceptibility values in the myocardium, water would be a convenient option as embedding media. As a drawback the influence of vibrational effects in the MRI must be mentioned, which leads to the fourth option, agarose [69].

With tissue embedded in agarose, movements and changes of the surrounding can be minimized. By changing the agarose' concentration, T2 relaxation times of human tissues can be mimicked [69]. This would avoid susceptibility jumps of the measured tissue at the borders.

Due to the hearts anatomy, it is hard to ensure an even distribution of the embedding media. Although galden has a high density and should fill all air regions, also in small vessels, not all regions might have been filled with the substance which led to local air bubbles and therefore artifacts in the susceptibility maps. Alternative methods could improve a better surrounding with a specific substance, for example cutting the heart in slices and placing it in a container. Similar tissue arrangement methods have been used for the brain [70]. This could lead to artifact removal due to a better embedding. However, the given experiments prove that the embedding media has influence on the calculated susceptibility values, which needs to be taken into account for the evaluation and comparison of future QSM studies.

6 Post-mortem application

6.1 Feasibility of PMMR

In past studies the feasibility of cardiac post-mortem MRI (PMMR) was evaluated as a method for investigating myocardial infarctions [37], and showed that post-mortem imaging can serve as an adjunct method of examination or also as an alternative technique for assessing cardiac pathologies [71]. Studies showed that PMMR can be used as a method for the examination of acute, subacute and chronic infarction [72, 73, 36, 74]. With the emergence of new techniques the traditional autopsies may be extended and supported by newer methods which deliver more insight into forensic issues [37]. With PMMR acquisition duration is not as critical as in clinical practice, meaning sequences with a better image resolution can be obtained.

Cardiac post-mortem MRI is affected by many factors, for example delay before imaging, time of survival and temperature, which all lead to different appearances of myocardial infarction. To use post-mortem imaging as a detection method, variables need to be systematically examined to receive robust and reliable results [71].

A general difficulty during pathological examination is the identification of peracute infarctions, because these are often not visible on macroscopic histological examinations [36]. The use of post-mortem MRI could be a way to improve pathological examinations and therefore achieve a better detection of peracute infarctions[37].

6.2 Detection of intramyocardial hemorrhage using QSM

Intramyocardial hemorrhage, which often accompanies acute myocardial infarction, can be detected with $T2$ or $T2^*$ cardiovascular magnetic resonance (CMR) [36]. In a hemorrhage the state of the hemoglobin has different effects on T2 relaxation time. Hemoglobin can be differentiated in oxyhemoglobin, deoxyhemoglobin, methemoglobins and hemichromes. Depending on different electronic structures (no unpaired electrons, diamagnetic, unpaired electrons, paramagnetic) of the hemoglobin types, the hemoglobin types have different magnetic susceptibility properties. Oxyhemoglobin and hemichromes are diamagnetic, whereas deoxy- and methemoglobin are paramagnetic. Superparamagnetic properties are shown by ferritin and hemosiderin [1, 2], which are breakdown products after red cell lysis [75]. This means that with increasing levels of deoxyhemoglobin also the magnetic susceptibility increases [76].

As by blood degeneration the hemoglobin within the hemorrhage changes, the infarcted tissue is hypointense on T2w and T2*w images, due to shortening of the relaxation times based on paramagnetic products [71, 77]. Another way to detect hemorrhages is to use filtered MRI phase data combined with magnitude data known as susceptibility weighted MRI images (SWI). Although SWI seems to be superior to T2*w imaging, it might not be specific enough as a method for finding myocardial infarction related changes in the myocardium [77].

In hemorrhagic myocardial infarction T2* relaxation is affected by the iron content in the hemorrhage, as well as present edema and fibrosis indicating that T2*w imaging may not function as a specific marker [78, 2, 79]. Recent work presented at the ISMRM2018 also deals with the subject of hemorrhagic myocardial infarction and QSM. A comparison to relaxation time mapping showed that QSM is a more specific marker for myocardial iron content and therefore can serve as an investigation method for hemorrhagic myocardial infarction. The infarcted tissue showed increased susceptibility values compared to the remote myocardium, correlating with elevated iron levels in the underlying tissue. The study shows the feasibility of QSM to serve as a method for investigating myocardial infarction [79].

7 Conclusion

Summarizing, the detection of hemorrhagic myocardial infarction and small tissue alterations in the myocardium is complex and challenging. With the emergence of newer MRI contrast and quantitative techniques such as Quantitative Susceptibility Mapping, new doors are opening up. Although recent findings are promising, the topic requires further research. To serve as an established post-mortem application the QSM algorithm needs to perform stable to ensure a reproducible, precise and accurate result. The presented work is a feasibility study of QSM investigating the myocardium. By using different sequences recently developed QSM algorithms were inspected in different aspects. The basis was built on phantom and ex situ porcine hearts acquisitions, which lead to an comparison of three recent QSM algorithms to investigate their accuracy, precision and stability depending on the input sequence. Further, the influence of four different embedding medias on the quantitative susceptibility maps was investigated.

In latest published QSM literature, mainly brain acquisitions, the susceptibility values are often reported with respect to a reference region. In the brain, QSM can be used to monitore tissue specific parameters as myelin or iron, which are indicators for neurological diseases. Experiments showed that for example the CSF region is known as a good reference [80, 81]. This rises the question, how reliable, meaningful and comparable are reported susceptibility values when they are not referenced to a specific region? Due to less research regarding cardiac or myocardial QSM acquisitions there is no established reference region as there is for the brain. For a better comparison of susceptibility values, an approach could be having a piece with known susceptibility, for example a vial filled with magnevist solution, next to the desired object during the MRI acquisition. Afterwards when calculating the quantitative susceptibility values, a masked area can be taken

into account as a reference. Nevertheless, the long term goal are stable and reliable algorithms leading to comparable susceptibility values.

As an established method, the whole QSM workflow should be automated and easy to use, where the number of manual steps needs to be minimized. For masking the tissue, the free segmentation tool by ITK-Snap led quickly and easily to the desired result. Chapter 4 showed that there is still work to do in algorithm development in stability and artifacts. Presented experiments demonstrated that the TGV algorithm [31, 32] is superior to the MEDI and starQSM algorithm. Further, the choice of the sequence can have an impact on the stability of the acquisition. Although the EPI sequence seemed to be unreliable for QSM, further experiments with varying sequence parameters can improve the reliability of the sequence for using it in QSM. The experiments in Chapter 5 prove that there is an impact on the magnetic susceptibility in the myocardium when embedded in different medias. However, there are still open questions as the reliability of comparing absolute values without referencing.

Nevertheless, the given experiments prove that a recent developed QSM algorithm, TGV algorithm, can work precise and reliable, with a good repeatability and reproducibility, but with the necessity to improve in terms of accuracy. As there are many positive findings with QSM used for the brain [82, 80], QSM for the myocardium is not evaluated so well but is still promising to be used as a tissue specific marker [3, 57]. The objective of the presented work was to provide a summary of recent QSM algorithms with experiments to get an insight on QSM as an application for myocardial tissue. It has the potential to reveal changes in hemoglobin states and therefore serve as a marker for hemorrhages which often accompanies myocardial infarction. With further research and developement in QSM algorithms and experiments for improving sequence parameters, quantitative susceptibility mapping can uncover the underlying tissue magnetic property and therefore serve as a method for assessing myocardial tissue alterations in the future.

Appendix

Bibliography

[1] E. L. AD Elster. : MRI of Hemorrhage: Overview, The appearance of hemorrhage on MRI seems very complicated. Can you simplify it? (2018). URL: http://mriquestions.com/hematoma-overview.html (visited on 08/22/2018) (cit. on pp. 3, 64).

[2] D. P. O'Regan, R. Ahmed, et al. : Reperfusion Hemorrhage Following Acute Myocardial Infarction: Assessment with T2* Mapping and Effect on Measuring the Area at Risk. *Radiology* 250.3 (2009), 916–922. DOI: 10.1148/radiol.2503081154 (cit. on pp. 3, 64).

[3] R. Dibb, Y. Qi, et al. : Magnetic susceptibility anisotropy of myocardium imaged by cardiovascular magnetic resonance reflects the anisotropy of myocardial filament α-helix polypeptide bonds. *Journal of Cardiovascular Magnetic Resonance* 17.1 (2015), 60–. DOI: 10.1186/s12968-015-0159-4 (cit. on pp. 3, 22, 66).

[4] F. Schweser, A. Deistung, et al. : Quantitative imaging of intrinsic magnetic tissue properties using MRI signal phase: An approach to in vivo brain iron metabolism? *NeuroImage* 54.4 (2011), 2789–2807. DOI: 10.1016/j.neuroimage.2010.10.070 (cit. on p. 4).

[5] de Rochefort Ludovic, N. Thanh, et al. : In vivo quantification of contrast agent concentration using the induced magnetic field for time-resolved arterial input function measurement with MRI. *Med. Phys.* 35.12 (2008), 5328–5339. DOI: 10.1118/1.3002309 (cit. on p. 4).

[6] J. Liu, T. Liu, et al. : Morphology Enabled Dipole Inversion for Quantitative Susceptibility Mapping Using Structural Consistency Between the Magnitude Image and the Susceptibility Map. *Neuroimage* 59.3 (2012), 2560–2568. DOI: 10.1016/j.neuroimage.2011.08.082 (cit. on pp. 4, 13, 18).

[7] F. Schweser, A. Deistung, et al. : Foundations of MRI phase imaging and processing for Quantitative Susceptibility Mapping (QSM). *Zeitschrift für Medizinische Physik* 26.1 (2016), 6–34. DOI: 10.1016/j.zemedi.2015.10.002 (cit. on pp. 4, 5).

[8] A. Rauscher, J. Sedlacik, et al. : Magnetic Susceptibility-Weighted MR Phase Imaging of the Human Brain. *Am. J. Neuroradiol.* 26.4 (2005), 736 (cit. on p. 5).

[9] F. S. John. : The role of magnetic susceptibility in magnetic resonance imaging: MRI magnetic compatibility of the first and second kinds. *Med. Phys.* 23.6 (1998), 815–850. DOI: 10.1118/1.597854 (cit. on p. 5).

[10] C. Westbrook, C. K. Roth, et al. *MRI in Practice*. 4th ed. Wiley, (2011). Chap. 9 - Instrumentation and equipment (cit. on p. 5).

[11] D. W. McRobbie, E. A. Moore, et al. : Seeing is believing: introduction to image contrast. In: *MRI from Picture to Proton*. 2nd ed. Cambridge: Cambridge University Press, (2006), 30–46. DOI: 10.1017/cbo9780511545405.003 (cit. on p. 5).

[12] R. Grinter. *The Quantum in Chemistry: An Experimentalist's View*. Wiley, (2005), pp. – (cit. on p. 5).

[13] E. M. Haacke, N. Y. C. Cheng, et al. : Imaging iron stores in the brain using magnetic resonance imaging. *Magnetic Resonance Imaging* 23.1 (2005), 1–25. DOI: 10.1016/j.mri.2004.10.001 (cit. on p. 6).

[14] B. Kressler, L. de Rochefort, et al. : Nonlinear Regularization for Per Voxel Estimation of Magnetic Susceptibility Distributions from MRI Field Maps. *IEEE transactions on medical imaging* 29.PMC2874210 (2010), 273–281. DOI: 10.1109/TMI.2009.2023787 (cit. on p. 6).

[15] L. Tian, S. Pascal, et al. : Calculation of susceptibility through multiple orientation sampling (COSMOS): A method for conditioning the inverse problem from measured magnetic field map to susceptibility source image in MRI. *Magn. Reson. Med.* 61.1 (2009), 196–204. DOI: 10.1002/mrm.21828 (cit. on p. 6).

[16] K. Shmueli, J. A. de Zwart, et al. : Magnetic Susceptibility Mapping of Brain Tissue In Vivo Using MRI Phase Data. *Magnetic resonance in medicine : official journal of the Society of Magnetic Resonance in Medicine / Society of Magnetic Resonance in Medicine* 62.PMC4275127 (2009), 1510–1522. DOI: 10.1002/mrm.22135 (cit. on p. 6).

[17] W. Sam, S. Andreas, et al. : Susceptibility mapping in the human brain using threshold-based k-space division. *Magn. Reson. Med.* 63.5 (2010), 1292–1304. DOI: 10.1002/mrm.22334 (cit. on p. 6).

[18] D. D. Bel and D. Y. et al. : Echo time. URL: https://radiopaedia.org/articles/echo-time (visited on 04/24/2018) (cit. on p. 9).

[19] D. D. Bel and D. Y. et al. : Flip angle. URL: https://radiopaedia.org/articles/flip-angle (visited on 04/24/2018) (cit. on p. 9).

[20] C. Westbrook, C. K. Roth, et al. *MRI in Practice*. 4th ed. Wiley, (2011). Chap. 5 -Pulse sequences (cit. on p. 9).

[21] L. Axel. : Glossary of MR Terms. American College of Radiology. *Magnetic resonance imaging* 5.3 (1987), 163–164 (cit. on p. 9).

[22] D. W. McRobbie, E. A. Moore, et al. : Getting in tune: resonance and relaxation. In: *MRI from Picture to Proton*. 2nd ed. Cambridge: Cambridge University Press, (2006), 137–166. DOI: 10.1017/cbo9780511545405.008 (cit. on pp. 10, 11).

[23] D. W. McRobbie, E. A. Moore, et al. : Spaced out: spatial encoding. In: *MRI from Picture to Proton*. 2nd ed. Cambridge: Cambridge University Press, (2006), 108–136. DOI: 10.1017/cbo9780511545405.007 (cit. on pp. 10, 11).

[24] D. G. Nishimura. *Principles of Magnetic Resonance Imaging*. (2011). Chap. 7 - Imaging Considerations (cit. on p. 10).

[25] E. L. AD Elster. : GRE vs SE. (2017). URL: http://mri-q.com/gre-vs-se.html (visited on 04/08/2018) (cit. on p. 10).

[26] D. W. McRobbie, E. A. Moore, et al. : Acronyms anonymous: a guide to the pulse sequence jungle. In: *MRI from Picture to Proton*. 2nd ed. Cambridge: Cambridge University Press, (2006), 220–257. DOI: 10.1017/cbo9780511545405.012 (cit. on p. 12).

[27] A. Elster. : Echoplanar-Imaging. (2017). URL: http://mriquestions.com/echo-planar-imaging.html (visited on 04/20/2018) (cit. on p. 12).

[28] M. A. Bernstein, K. F. King, et al. : Chapter 16 - Echo Train Pulse Sequences. In: *Handbook of MRI Pulse Sequences*. Burlington: Academic Press, (2004), 702–801 (cit. on p. 12).

[29] de Rochefort Ludovic, L. Tian, et al. : Quantitative susceptibility map reconstruction from MR phase data using bayesian regularization: Validation and application to brain imaging. *Magn. Reson. Med.* 63.1 (2009), 194–206. DOI: 10.1002/mrm.22187 (cit. on pp. 13, 18).

[30] H. Wei, R. Dibb, et al. : Streaking Artifact Reduction for Quantitative Susceptibility Mapping of Sources with Large Dynamic Range. *NMR in biomedicine* 28.10 (2015), 1294–1303. DOI: 10.1002/nbm.3383 (cit. on pp. 13, 19, 22, 47, 49).

[31] K. Bredies, K. Kunisch, et al. : Total Generalized Variation. *SIAM J. Imaging Sci.* 3.3 (2010), 492–526. DOI: 10.1137/090769521 (cit. on pp. 13, 20, 66).

[32] C. Langkammer, K. Bredies, et al. : Fast quantitative susceptibility mapping using 3D EPI and total generalized variation. *NeuroImage* 111.Supplement C (2015), 622–630. DOI: 10.1016/j.neuroimage.2015.02.041 (cit. on pp. 13, 20, 49, 66).

[33] SimpleElastix. URL: https://simpleelastix.github.io/ (cit. on pp. 15, 16, 56).

[34] P. A. Yushkevich, J. Piven, et al. : User-guided 3D active contour segmentation of anatomical structures: Significantly improved efficiency and reliability. *NeuroImage* 31.3 (2006). http://www.itksnap.org/, 1116–1128 (cit. on pp. 15–17).

[35] B. M. Webb. "Post-mortem MR imaging techniques for the assessment of sudden cardiac death: Quantitative and angiography-based approaches." PhD thesis. TU Graz, Institut für Medizintechnik, 2018 (cit. on pp. 15, 25, 46).

[36] C. Jackowski, N. Schwendener, et al. : Post-Mortem Cardiac 3-T Magnetic Resonance Imaging: Visualization of Sudden Cardiac Death? *Journal of the American College of Cardiology* 62.7 (2013), 617–629. DOI: 10.1016/j.jacc.2013.01.089 (cit. on pp. 15, 63, 64).

[37] C. Jackowski, A. Christe, et al. : Postmortem unenhanced magnetic resonance imaging of myocardial infarction in correlation to histological infarction age characterization. *European Heart Journal* 27.20 (2006), 2459–2467. DOI: 10.1093/eurheartj/ehl255 (cit. on pp. 15, 63).

[38] G. Thallinger. : Biostatistics and Experimental Design. Lecture. (2015/2016). URL: https://online.tugraz.at/tug_online/wbLv.wbShowLVDetail?pStpSpNr=191964 (cit. on p. 17).

[39] T. Liu, I. Khalidov, et al. : A novel background field removal method for MRI using projection onto dipole fields (PDF). *NMR in biomedicine* 24.PMC3628923 (2011), 1129–1136. DOI: 10.1002/nbm.1670 (cit. on p. 18).

[40] Z. Liu, P. Spincemaille, et al. : MEDI+0: Morphology enabled dipole inversion with automatic uniform cerebrospinal fluid zero reference for quantitative susceptibility mapping. *Magn. Reson. Med.* 79.5 (2018), 2795–2803. DOI: 10.1002/mrm.26946 (cit. on p. 18).

[41] T. Liu, C. Wisnieff, et al. : Nonlinear formulation of the magnetic field to source relationship for robust quantitative susceptibility mapping. *Magn Reson Med* 69.2 (2013), 467–476. DOI: 10.1002/mrm.24272 (cit. on p. 18).

[42] T. Liu, J. Liu, et al. : Morphology enabled dipole inversion (MEDI) from a single-angle acquisition: Comparison with COSMOS in human brain imaging. *Magn. Reson. Med.* 66.3 (2011), 777–783. DOI: 10.1002/mrm.22816 (cit. on p. 18).

[43] W. Li, B. Wu, et al. : Quantitative Susceptibility Mapping of Human Brain Reflects Spatial Variation in Tissue Composition. *NeuroImage* 55.PMC3062654 (2011), 1645–1656. DOI: 10.1016/j.neuroimage.2010.11.088 (cit. on p. 19).

[44] B. Wu, W. Li, et al. : Whole Brain Susceptibility Mapping Using Compressed Sensing. *Magnetic resonance in medicine : official journal of the Society of Magnetic Resonance in Medicine / Society of Magnetic Resonance in Medicine* 67.PMC3249423 (2011), 137–147. DOI: 10.1002/mrm.23000 (cit. on p. 19).

[45] H. Wei, R. Dibb, et al. : Investigating magnetic susceptibility of human knee joint at 7 Tesla. *Magn. Reson. Med* 78.5 (2017), 1933–1943. DOI: 10.1002/mrm.26596 (cit. on p. 19).

[46] E. Olsson, R. Wirestam, et al. : MRI-Based Quantification of Magnetic Susceptibility in Gel Phantoms: Assessment of Measurement and Calculation Accuracy. *Radiology Research and Practice* 2018 (2018), 13. DOI: 10.1155/2018/6709525 (cit. on pp. 22, 48, 49).

[47] Bayer-Vital. URL: https://www.patienteninfo-service.de/a-z-liste/m/magnevistR-05-mmolml-injektionsloesung/ (cit. on pp. 22, 32).

[48] L. de Rochefort, R. Brown, et al. : Quantitative MR susceptibility mapping using piece-wise constant regularized inversion of the magnetic field. *Magn. Reson. Med.* 60.4 (2008), 1003–1009. DOI: 10.1002/mrm.21710 (cit. on p. 22).

[49] O. Dietrich, J. G. Raya, et al. : Measurement of signal-to-noise ratios in MR images: Influence of multichannel coils, parallel imaging, and reconstruction filters. *J. Magn. Reson. Imaging* 26.2 (2007), 375–385. DOI: 10.1002/jmri.20969 (cit. on pp. 23, 24).

[50] J. M. Bland and D. G. Altman. : Agreement Between Methods of Measurement with Multiple Observations Per Individual. *Journal of Biopharmaceutical Statistics* 17.4 (2007), 571–582. DOI: 10.1080/10543400701329422 (cit. on p. 24).

[51] R. R. Ernst and W. A. Anderson. *Application of Fourier Transform Spectroscopy to Magnetic Resonance*. Vol. 37. (1966), pp. 93–102. DOI: 10.1063/1.1719961 (cit. on p. 46).

[52] Y. Wang and T. Liu. : Quantitative susceptibility mapping (QSM): Decoding MRI data for a tissue magnetic biomarker. *Magnetic Resonance in Medicine* 73.PMC4297605 (2014), 82–101. DOI: 10.1002/mrm.25358 (cit. on p. 46).

[53] C. D. Jordan, B. L. Daniel, et al. : Subject-Specific Models of Susceptibility-Induced B(0) Field Variations in Breast MRI. *Journal of magnetic resonance imaging : JMRI* 37.PMC3492544 (2012), 227–232. DOI: 10.1002/jmri.23762 (cit. on p. 47).

[54] C. Liu, W. Li, et al. : Susceptibility-Weighted Imaging and Quantitative Susceptibility Mapping in the Brain. *Journal of magnetic resonance imaging : JMRI* 42.PMC4406874 (2014), 23–41. DOI: 10.1002/jmri.24768 (cit. on p. 47).

[55] T. Liu, W. Xu, et al. : Accuracy of the Morphology Enabled Dipole Inversion (MEDI) Algorithm for Quantitative Susceptibility Mapping in MRI. *IEEE transactions on medical imaging* 31.3 (2012), 816–824. DOI: 10.1109/TMI.2011.2182523 (cit. on pp. 47–49).

[56] C. Wisnieff, T. Liu, et al. : Magnetic susceptibility anisotropy: cylindrical symmetry from macroscopically ordered anisotropic molecules and accuracy of MRI measurements using few orientations. *NeuroImage* 70.PMC3580080 (2013), 363–376. DOI: 10.1016/j.neuroimage.2012.12.050 (cit. on p. 49).

[57] R. Dibb, L. Xie, et al. : Magnetic susceptibility anisotropy outside the central nervous system. *NMR Biomed.* 30.4 (2017), e3544–n/a. DOI: 10.1002/nbm.3544 (cit. on pp. 50, 66).

[58] J. Peter and S. Balaban Robert. : Correction for geometric distortion in echo planar images from Bo field variations. *Magn. Reson. Med.* 34.1 (1995), 65–73. DOI: 10.1002/mrm.1910340111 (cit. on p. 53).

[59] M. Poustchi-Amin, S. A. Mirowitz, et al. : Principles and Applications of Echo-planar Imaging: A Review for the General Radiologist. *RadioGraphics* 21.3 (2001), 767–779. DOI: 10.1148/radiographics.21.3.g01ma23767 (cit. on p. 53).

[60] Q. X. Yang, J. Wang, et al. : Reduction of magnetic field inhomogeneity artifacts in echo planar imaging with SENSE and GESEPI at high field. *Magn. Reson. Med.* 52.6 (2004), 1418–1423. DOI: 10.1002/mrm.20303 (cit. on p. 53).

[61] W. Fishbein Kenneth, A. Gluzband Yehezkiel, et al. : Effects of formalin fixation and collagen cross-linking on T2 and magnetization transfer in bovine nasal cartilage. *Magn. Reson. Med.* 57.6 (2007), 1000–1011. DOI: 10.1002/mrm.21216 (cit. on p. 55).

[62] Solvay. : Galden PFPE Perfluoropolyether Fluorinated Fluids. 26.9.2018. URL: https://www.solvay.com/en/products/brands/galden-pfpe (cit. on p. 55).

[63] M. T. GmbH. URL: http://www.mascom-bremen.de/html/de/vakuum-erzeugung/vakuum-oele/sv55-cubitainer-5-kg-galden/article-1-SV55_.5KG-ONLINE_.SHOP90209020390-6.html (visited on 08/31/2018) (cit. on p. 56).

[64] P. Dusek, V. I. Madai, et al. "[unpublished] Differential impact of embedding media on R2* relaxation rate and QSM in post-mortem brain MRI at 7.0T" (cit. on pp. 57, 60).

[65] : Z-Score: Definition, Formula and Calculation. URL: http://www.statisticshowto.com/probability-and-statistics/z-score/ (visited on 08/31/2018) (cit. on p. 60).

[66] : Standard Score (cont...) URL: https://statistics.laerd.com/statistical-guides/standard-score-2.php (visited on 08/31/2018) (cit. on p. 60).

[67] D. Samartzis, F. H. Shen, et al. : Bone mineral density. URL: https://www.britannica.com/science/bone-mineral-density#ref1183633 (visited on 08/31/2018) (cit. on p. 60).

[68] R. Burgkart, C. Glaser, et al. : Feasibility of T and Z scores from magnetic resonance imaging data for quantification of cartilage loss in osteoarthritis. *Arthritis & Rheumatism* 48.10 (2003), 2829–2835. DOI: 10.1002/art.11259 (cit. on p. 60).

[69] A. Hellerbach, V. Schuster, et al. : MRI Phantoms - Are There Alternatives to Agar? *PLoS ONE* 8.PMC3734012 (2013). Ed. by C. Oreja-Guevara, e70343. DOI: 10.1371/journal.pone.0070343 (cit. on p. 61).

[70] C. Langkammer, N. Krebs, et al. : Susceptibility induced gray-white matter MRI contrast in the human brain. *Neuroimage* 59.2-5 (2011), 1413–1419. DOI: 10.1016/j.neuroimage.2011.08.045 (cit. on p. 61).

[71] C. Jackowski, W. Schweitzer, et al. : Virtopsy: postmortem imaging of the human heart in situ using MSCT and MRI. *Forensic Science International* 149.1 (2005), 11–23. DOI: 10.1016/j.forsciint.2004.05.019 (cit. on pp. 63, 64).

[72] E. J. Ulbrich, R. Sutter, et al. : STIR Sequence With Increased Receiver Bandwidth of the Inversion Pulse for Reduction of Metallic Artifacts. *American Journal of Roentgenology* 199.6 (2012), W735–W742. DOI: 10.2214/ajr.11.8233 (cit. on p. 63).

[73] C. Jackowski, M. J. B. Warntjes, et al. : Magnetic resonance imaging goes postmortem: noninvasive detection and assessment of myocardial infarction by postmortem MRI. *European Radiology* 21.1 (2011), 70–78. DOI: 10.1007/s00330-010-1884-6 (cit. on p. 63).

[74] T. D. Ruder, M. J. Thali, et al. : Essentials of forensic post-mortem MR imaging in adults. *The British Journal of Radiology* 87.PMC4067017 (2013), 20130567. DOI: 10.1259/bjr.20130567 (cit. on p. 63).

[75] W. G. Bradley. : MR appearance of hemorrhage in the brain. *Radiology* 189.1 (1993), 15–26. DOI: 10.1148/radiology.189.1.8372185 (cit. on p. 64).

[76] J. Zhang, T. Liu, et al. : Quantitative Mapping of Cerebral Metabolic Rate of Oxygen (CMRO(2)) using Quantitative Susceptibility Mapping (QSM). *Magnetic resonance in medicine* 74.PMC4375095 (2014), 945–952. DOI: 10.1002/mrm.25463 (cit. on p. 64).

[77] A. Kidambi, J. D. Biglands, et al. : Susceptibility-weighted cardiovascular magnetic resonance in comparison to T2 and T2 star imaging for detection of intramyocardial hemorrhage following acute myocardial infarction at 3 Tesla. *Journal of Cardiovascular Magnetic Resonance* 16.PMC4210544 (2014), 86. DOI: 10.1186/s12968-014-0086-9 (cit. on p. 64).

[78] N. R. Ghugre, V. Ramanan, et al. : Quantitative tracking of edema, hemorrhage, and microvascular obstruction in subacute myocardial infarction in a porcine model by MRI. *Magn. Reson. Med.* 66.4 (2011), 1129–1141. DOI: 10.1002/mrm.22855 (cit. on p. 64).

[79] B. F. Moon, S. K. Iyer, et al. "[unpublished] Magnetic susceptibility of hemorrhagic myocardial infarction: correlation with tissue iron and comparison with relaxation time MRI." 2018 (cit. on p. 64).

[80] X. Feng, A. Deistung, et al. : Quantitative susceptibility mapping (QSM) and R2* in the human brain at 3T: Evaluation of intra-scanner repeatability. *Zeitschrift für Medizinische Physik* 28.1 (2018), 36–48. DOI: 10.1016/j.zemedi.2017.05.003 (cit. on pp. 65, 66).

[81] S. Straub, T. M. Schneider, et al. : Suitable reference tissues for quantitative susceptibility mapping of the brain. *Magn. Reson. Med.* 78.1 (2017), 204–214. DOI: 10.1002/mrm.26369 (cit. on p. 65).

[82] C. Langkammer, L. Pirpamer, et al. : Quantitative Susceptibility Mapping in Parkinson's Disease. *PLoS ONE* 11.9 (2016), e0162460–. DOI: 10.1371/journal.pone.0162460 (cit. on p. 66).